

DNA actively regulates the “safety-belt” dynamics of condensin during loop extrusion

Received: 10 May 2025

Accepted: 18 December 2025

Cite this article as: Chen, J., Feng, C., Wang, Y. *et al.* DNA actively regulates the “safety-belt” dynamics of condensin during loop extrusion. *Nat Commun* (2025). <https://doi.org/10.1038/s41467-025-68239-6>

Jinyu Chen, Cibo Feng, Yong Wang & Xiakun Chu

We are providing an unedited version of this manuscript to give early access to its findings. Before final publication, the manuscript will undergo further editing. Please note there may be errors present which affect the content, and all legal disclaimers apply.

If this paper is publishing under a Transparent Peer Review model then Peer Review reports will publish with the final article.

DNA Actively Regulates the “Safety-Belt” Dynamics of Condensin during Loop Extrusion

Jinyu Chen¹, Cibo Feng¹, Yong Wang², and Xiakun Chu^{1,3,*}

¹Advanced Materials Thrust, Function Hub, The Hong Kong University of Science and Technology (Guangzhou), Guangzhou 511400, China

²College of Life Sciences, Zhejiang University, Hangzhou, 310027, China

³Guangzhou Municipal Key Laboratory of Materials Informatics, The Hong Kong University of Science and Technology (Guangzhou), Guangzhou 511400, China

*Email: xiakunchu@hkust-gz.edu.cn

Abstract

Condensin plays an essential role in genome folding through its active DNA loop extrusion activity. Condensin contains a binding interface between its Ycg1 HEAT-repeat subunit and the Brn1 kleisin, together forming a “safety-belt” DNA-binding groove. This safety-belt architecture traps DNA inside the structural maintenance of chromosomes complex and prevents its dissociation during loop extrusion. The entrapment of DNA within the binding pocket of the complex is crucial for ATPase activity and loop extrusion. However, the molecular mechanism underlying DNA entrapment remains unclear. Here, we employ a multiscale computational approach to understand how DNA modulates yeast condensin’s safety-belt dynamics. Using all-atom simulations combined with AlphaFold3 predictions, we demonstrate that DNA binding stabilizes the Ycg1-Brn1 safety belt. Coarse-grained simulations capture the entire DNA-entrapment process and reveal an active regulatory role for DNA: outside the safety belt, DNA triggers opening, whereas once inside, it promotes closure and stabilizes the complex. Kinetic analyses show that the rate-limiting step in DNA entrapment depends on the tightness of the safety belt. A loose safety belt makes the stable closure of its “latch” and “buckle” components rate-limiting, whereas a tighter safety belt shifts the barrier to initial DNA entry.

Introduction

Mitosis and meiosis are fundamental processes of eukaryotic cell division. During these processes, the stable and orderly transmission of genetic information is crucial for maintaining species continuity and the proper develop-

ment of organisms [1, 2, 3]. The spatial organization of chromosomes is of paramount importance in mitosis, and achieving this organization relies on structural maintenance of chromosomes (SMC) complexes, such as condensin.

Condensin, a five-subunit complex of the SMC family, plays a vital role in condensation and segregation during this process [4, 5, 6]. It is primarily composed of two key parts: the “SMC dimers” subcomplex and the “non-SMC” subcomplex [7]. The SMC dimers subcomplex consists of a heterodimer formed by SMC2 and SMC4 subunits, and the non-SMC subcomplex composed of the kleisin subunit and two HEAT-repeat subunits [8]. Together, these two subcomplexes enable condensin to compact chromatin into highly ordered structures necessary for faithful chromosome segregation. Condensin has long been recognized as a pivotal player in mitotic chromosome assembly. However, the precise mechanism by which it compacts and organizes DNA remains unclear. Several models have been proposed over the years, and a simple and elegant mechanism that could explain most of the cellular tasks of SMC complexes called “loop extrusion” is one of the most widely accepted [9, 10, 11, 12, 13, 4, 14].

Condensin complexes are characterized by conformational changes coupled with the ATP hydrolysis cycle and facilitate the lengthwise compaction of DNA through ATPase-driven loop extrusion [15, 12, 16, 17, 18, 19, 20]. Current research indicates that condensin contains multiple DNA-binding interfaces [21]. A safety-belt mechanism, as revealed by DNA-condensin co-crystal structures, indicates that DNA is confined within a conserved, positively charged groove formed by *Saccharomyces cerevisiae* (Sc) condensin Ycg1 HEAT-repeat and Brn1 kleisin subunits and is restricted by a ring-shaped Brn1 loop of the non-SMC subcomplex (Figures 1A and 1B) [22]. In ATP-

engaged states, DNA is also clamped at the SMC2/SMC4 head module in conjunction with Ycs4 HEAT-repeat subunit, indicating that both the non-SMC subunits and the SMC heads contribute to DNA binding [21]. These interfaces have been observed across the SMC cycle and are consistent with models in which condensin captures and transports DNA during loop extrusion [14]. The observation that DNA binding by the non-SMC subcomplex of condensin decisively enhances the activity of the SMC ATPase indicates that a multistep mechanism is involved in the loading of condensin onto chromosomes. This implies that the DNA binding site in the non-SMC subcomplex might be able to act as a sensor that triggers activation of the SMC2-SMC4 ATPase [23]. The initial step in the condensin loading mechanism involves the binding of DNA to the non-SMC subcomplex, a process that is thought to occur independently of ATP hydrolysis [24]. A disruption in the interaction between DNA and the non-SMC subcomplex markedly affects condensin loading efficiency, underscoring the critical role of this interface in DNA recognition [23].

DNA entrapment by the Brn1 loop and its subsequent closure around the DNA double helix via the safety-belt mechanism are critical for stable condensin-DNA engagement [22, 23]. Although DNA can access the basic Ycg1-Brn1 groove without being encircled by the Brn1 loop, it is only through the latch-mediated entrapment that the affinity is sufficiently increased to enable stable interaction with chromatin [22]. Since the "latch" and "buckle" segments can engage with each other even without DNA, the latch must temporarily disengage from the buckle to allow DNA to enter the Brn1 kleisin loop [22]. However, if the safety belt opens too rarely, DNA would seldom be captured, making loop extrusion inefficient. Conversely, if it opens too easily or frequently, the condensin complex might become unstable (losing DNA or failing to maintain ATPase engagement). Therefore, understanding how the safety-belt mechanism achieves a balance between effective DNA entrapment and structural stability is essential for elucidating its functional mechanism.

Previous studies have suggested, based on biochemical and structural evidence, that cohesin and condensin may topologically encircle DNA [25, 26, 27, 28, 29, 30, 31]. However, experiments also showed that simultaneous closure of all three SMC-kleisin ring interfaces does not inhibit DNA loop extrusion by cohesin and condensin. This finding challenges the hypothesis that DNA passes through the SMC-kleisin ring in a strictly topological manner [11, 15]. In the "hold-and-feed" model, condensin is proposed to load DNA into the SMC-kleisin ring in a "pseudotopological" manner. In this scenario, the DNA is topologically entrapped within two distinct kleisin compartments, referred to as the "motor" and "anchor" chambers [15]. The topologically bound DNA segments within

the safety belt during the SMC reaction cycle are thought to determine the directionality of DNA loop extrusion. A recent study suggested that both cohesin and condensin are believed to extrude DNA loops in an asymmetric manner, and the frequent switching of extrusion direction has been proposed as a possible explanation for the experimentally observed symmetric loop extrusion [9]. Notably, if the barrier between the "motor" and "anchor" chambers is removed (allowing them to connect), condensin could theoretically extrude DNA in both directions instead of one, essentially converting it from a one-sided to a two-sided loop extruder. Therefore, a detailed understanding of the safety-belt mechanism may provide important insights into the mechanistic differences in loop extrusion between condensin and cohesin.

Single-molecule and structural studies have established that condensin and cohesin compact DNA by ATP-dependent loop extrusion, placing SMCs at the center of 3D genome architecture [10, 32, 11]. Within this framework, capture and entrapment of DNA are key control points. In Sc condensin, the kleisin-HEAT "safety-belt" forms a positively charged groove and a ring-like Brn1 loop that can encircle DNA and prevent dissociation, providing a structural basis for anchoring and the one-sided loop growth observed for condensin [22, 10]. Thus, local protein-DNA mechanics at the safety belt connect directly to long-range chromosome organization. The established principle that condensin's safety belt couples local DNA mechanics to chromosome organization motivates exploration of whether analogous DNA-clamping mechanisms operate in other SMC complexes. Structural work on budding-yeast cohesin has revealed a "safety-belt-like" Scc3-Scc1 DNA-binding interface, supporting the idea that secure DNA latching by non-SMC subunits may represent a conserved biophysical strategy, even if the underlying architectures differ [33]. By contrast, the Smc5/6 complex lacks canonical HEAT-repeat subunits and instead employs KITE-family non-SMC elements, implying a distinct mode of DNA interaction [34]. A detailed investigation of condensin's DNA capture and latch stability is therefore well placed to inform mechanistic models across the SMC family, while also clarifying which features are specific to condensin. Finally, SMC dysfunction has biomedical impact: cohesin alterations are frequent in human cancers and associate with transcriptional dysregulation and chromatin changes, underscoring the importance of clarifying SMC-mediated DNA capture and control [35, 36].

Recent advances in AI-based protein structure prediction methods, such as AlphaFold [37, 38], have enabled computational exploration of protein conformational diversity. Further studies have demonstrated that these predictive models can not only accurately reproduce experimentally determined static structures but also sample mul-

multiple conformational states by adjusting input parameters [39, 40]. Two confidence/readout scores are especially useful for interpreting such ensembles: the predicted local distance difference test (pLDDT), a per-residue measure of local reliability, and the predicted aligned error (PAE), a residue-pair measure of confidence in the relative placement of regions. Both scores correlate with intrinsic flexibility, helping to flag mobile segments and inter-domain motions [41, 42]. Moreover, structural changes predicted by AlphaFold have been successfully applied to assess the impact of single-point mutations on protein conformation, with results showing remarkable agreement with experiments [43, 44]. These findings highlight the potential of predicted scores in AlphaFold to capture aspects of protein dynamics, providing insights into conformational transitions and functional regulation.

Here, we integrate AlphaFold3-based predictions, all-atom and coarse-grained (CG) molecular dynamics (MD) simulations to study the conformational mechanisms of Sc condensin's Ycg1-Brn1 safety belt. This multiscale approach reconstructs the full DNA-entrapment pathway and delineates its intermediate states. We find that DNA acts bidirectionally: when positioned outside the Brn1 loop it biases the latch toward opening, whereas once inside it promotes latch-buckle closure and stabilizes the complex during ATPase cycling. Kinetic analyses show that the rate-limiting step depends on belt "tightness": weaker latch-buckle coupling makes closure limiting, whereas stronger coupling shifts the barrier to initial DNA entry. We further identify an optimal interaction regime that balances efficient capture with stable interface engagement, and we uncover a strong link between safety-belt stability and one-dimensional sliding along DNA. Together, these results provide a molecular framework for DNA-guided control of the safety belt and clarify how condensin achieves robust topological capture during loop extrusion.

Results

AlphaFold3 Predictions of Safety-Belt Flexibility in DNA-unbound state (US) and DNA-bound state (BS)

We first asked how the Sc Brn1 kleisin loop (residues 383-524) behaves in the DNA-bound state (BS) versus DNA-unbound state (US). To analyze its dynamics and identify functionally relevant conformational changes of Brn1 kleisin loop, we calculated the effective strain (ES) per residue, ES_i , as a measure of local flexibility, with higher ES indicating larger deformation (lower stability). This method is analogous to the local deformation concept from previous work [43], with the key difference being that we compute the normalized PAE for each aligned

residue i as $\langle ES_i \rangle = \langle PAE_{ij} / r_{ij} \rangle$ for all scored residues j within 13 Å averaged across all 10 predicted structures. Normalizing PAE by inter-residue distance removes the strong distance bias in raw PAE values, enabling fair comparisons across regions and interaction scales. Higher normalized PAE values indicate greater uncertainty in the placement of aligned residue i relative to scored residue j , whereas lower values indicate higher certainty. Consequently, a higher value of $\langle ES_i \rangle$ corresponds to increased flexibility in the local structural region, while a lower value of $\langle ES_i \rangle$ corresponds to decreased flexibility in the local structural region (see Methods for details). Before using PAE to derive effective strain measures, we verified that the AlphaFold3 models reproduce the known crystal structures of the Ycg1-Brn1 complex in the US and BS with backbone $C\alpha$ root-mean-square deviations (RMSDs) of 1.466 ± 0.047 Å and 0.795 ± 0.022 Å, respectively (Table S2). This supports the global accuracy of the AlphaFold3 models used here.

To assess whether the PAE-derived effective strain $\langle ES_i \rangle$ is a sensitive readout of local structural integrity within the safety belt, we modeled four latch mutations that were experimentally found to weaken latch-buckle engagement (M391D, F394D, W402D, W408D) and compared wild-type and mutant ensembles (Figure S1) [22]. For each variant, we computed change of effective strain upon mutation ($\Delta \langle ES_i \rangle$) and summarized the response by shell sums within 13, 15, and 18 Å of the mutated site. Three mutations (M391D, F394D, W402D) produced clear, localized increases in $\langle ES_i \rangle$, consistent with destabilization of latch-buckle contacts; W408D yielded a weaker negative response, likely because this residue lies near the boundary of robust PAE coverage in our models. These findings support $\langle ES_i \rangle$ as a practical indicator of mutation-induced strain at the safety-belt interface. More broadly, this provides internal validation for our PAE-based analysis and may offer a general, low-cost screen to prioritize residues for mechanistic tests that tune safety-belt dynamics and, by extension, loop-extrusion competence.

We then projected $\langle ES_i \rangle$ directly onto the structure of the Brn1 kleisin loop to clearly visualize the structural stability of the Brn1 kleisin loop (Figure 1A). The latch region of Brn1 exhibits markedly higher $\langle ES_i \rangle$ values, which is closely associated with the fact that the latch region serves as the primary functional area responsible for the opening and closing mechanism of the safety belt. To assess how the presence or absence of DNA influences safety-belt stability, we then projected $\langle ES_i(US) \rangle - \langle ES_i(BS) \rangle$ directly onto the structure of the Brn1 kleisin loop, thereby providing a direct visualization of DNA-induced changes in the structural stability of this region. Notably, $\langle ES_i(BS) \rangle$ values are markedly reduced compared with the $\langle ES_i(US) \rangle$ in the latch segment (~residues 383-410), indicating enhanced local stability (Figure 1B).

To understand why $\langle ES_i \rangle$ decreases upon DNA binding, we examined the pairwise strain matrix $\langle ES_{ij} \rangle$, which reports how confidently residue i is positioned relative to nearby residues j (derived from normalized PAE; see Methods). Across the latch region, $\langle ES_{ij} \rangle$ is substantially lower in the BS than US (Figure 1C), indicating a broad DNA-induced stabilization. A per-residue view of $\langle ES_i \rangle$ refines this picture (Figure 1D): the largest stabilization occurs in the flexible latch segment $\sim 383-410$, whereas intrinsically more rigid segments (lower normalized PAE) change less but follow the same overall trend. These patterns are robust to reasonable choices of the neighborhood cutoff and other analysis parameters (Figure S2). For completeness, $\langle ES_i \rangle$ and the matrices of $\langle ES_{ij} \rangle$ over the full Brn1 loop are provided in Figure S3.

Together, these findings suggest that DNA binding notably stabilizes a particular flexible segment of the Brn1 loop (residues 383-410), as indicated by a drop in the effective strain in the BS relative to the US. This segment corresponds to the latch region of the Brn1 safety-belt that closes around DNA. Regions that AlphaFold3 predicted to be highly flexible (those with larger prediction error) showed the greatest DNA-induced stabilization, whereas inherently rigid regions changed little. Our results suggest that DNA binding preferentially stabilizes the parts of the Brn1 loop that need to flex during latch opening and closing.

Insights into DNA-Stabilized Safety-Belt Mechanism from atomistic MD Simulations

The prediction results of local deformations suggest that the DNA entrapment by the safety belt can facilitate the closure of the Brn1 loop. As AlphaFold3 primarily provides static structural predictions, additional validation through MD simulations or experimental approaches is required to assess the conformational dynamics. To further investigate how the safety belt maintains structural stability following DNA entrapment, we constructed two simulation systems, one with DNA and one without, and then performed unbiased all-atom MD simulations on each. The BS was retrieved from the Protein Data Bank (PDB:5OQO) [22] and the US was generated by deleting DNA from the PDB. The missing residues in the crystal structure are reconstructed (see Methods for details). As shown in Figure 2A, we illustrate the key structural concepts within the complex, particularly the latch region, buckle region, and the primary active region (PAR, Brn1 residues 383-456, latch + linker). The pale-green segment marks the intrinsically disordered linker within the Brn1 loop, and the four Brn1 α -helices ($\alpha 1-\alpha 4$) are labeled for reference.

To quantitatively assess the structural dynamics of the Brn1 loop at the residue level in the presence and absence

of DNA, we first compared the residue-wise root-mean-square fluctuation (RMSF) within the US and BS. RMSF measures how much each residue moves during the simulation with higher (lower) RMSF corresponding to greater (weaker) flexibility. The RMSF profile of the US is generally larger than that of the BS, indicating that the presence of DNA within the Brn1 loop enhances the overall structural stability of the safety belt (Figure 2B). Notably, residues near position D424 in the BS show a modest increase in RMSF compared to the US. This results from a higher concentration of negatively charged residues in that region, which, together with the negative charge of the DNA helix, weakens local interactions at the protein-DNA interface. Figure 2C illustrates that the primary contributor to RMSF stabilization is the direct interaction between DNA and the PAR of the Brn1 loop. Moreover, the slightly higher contact number between the PAR and the rest of the protein (excluding DNA) in the BS suggests that DNA binding may indirectly stabilize adjacent structural regions.

Motivated by this observation, we next asked whether the DNA-induced "latch flipping" reported by Kschonsak et al. is evident in our MD simulations [22]. In that mechanism, DNA promotes a reorientation near Brn1 K409/R411 such that V410 packs with W408 (Brn1) and F808 (Ycg1), consolidating a small hydrophobic cluster at the latch-buckle interface. We therefore quantified side-chain centroid distances and contact probabilities for V410-F808 (hydrophobic packing) and R411-F808 (Arg reorientation) in the US and BS (Figure S4). In the BS, V410-F808 shifts toward shorter distances and higher contact probability, whereas R411-F808 shifts toward longer distances with a modest contact decrease. These reproducible BS-US differences are consistent with DNA-triggered latch flipping and local interface consolidation [22].

To pinpoint which amino acids at the latch-buckle interface change their energetic roles upon DNA binding, we applied an end-point free-energy decomposition (MM/GBSA) method on MD trajectories and ranked per-residue contributions (Figure S5) [45, 46]. We extracted the top contributors from three regions: the Brn1 latch (383-410), the Brn1 buckle (497-524), and Ycg1 residues within 0.4 nm of the latch. Overall, the leading latch residues remain important in both the US and BS. Notably, R400 and R405 provide more stabilizing contributions in BS, consistent with stronger electrostatic engagement with the DNA phosphate backbone in the DNA-bound architecture. Hydrophobic latch residues M391, F394, W402, and W408 also rank among the top stabilizers, aligning with experimental evidence that these sites help maintain latch-buckle integrity [22]. The Ycg1 buckle shows only modest rank shifts between states, whereas the presence of DNA broadens the set of Brn1 buckle residues that contact

and stabilize the interface, indicating a more extensively engaged latch-buckle surface in the BS.

The RMSF and contact number analyses from all-atom MD simulations showed that DNA stabilized the Brn1 loop by forming additional interactions. To further assess how this interaction influences latch disengagement from the buckle in the safety belt, we performed steered MD simulations, unraveling the safety belt in the US and BS. To preserve the flexibility of the buckle region at its interface with the latch region while preventing large-scale translations or rotations of the buckle region, positional restraints were applied to atoms of the Ycg1 subunit that do not directly interact with the PAR (see Figure S6 and Methods for details). We present the average force profiles as a function of the z-axis distance between the centers of mass (COMs) of the first $C\alpha$ atom of the latch region of the Brn1 loop and Ycg1 subunits, derived from three independent steered MD simulations. Notably, the BS exhibits generally higher force values compared to the US (Figure 2D). The results indicate that DNA enhances the interaction network at the interface, leading to an increased force required for latch release. The presence of DNA stabilizes the interaction between the latch and buckle, making the Brn1 loop less likely to open. This stability is important for the safety-belt function and subsequent ATP hydrolysis. In the steered MD process, the latch region is pulled by a force at constant velocity, leading to its gradual detachment from the buckle region. The changes in the contact number between the PAR and the remaining part during this process are shown in Figure 2E. Even under steered MD, the comparison of contact numbers between the US and BS remains highly correlated with the presence or absence of DNA near the crystal structure in the unbiased simulation. The difference in contact number between the US and BS comes mainly from the contact between DNA and the PAR. Quantitative analysis of contact numbers reveals comparable interaction profiles between the US and BS when excluding contacts between DNA and the PAR of the Brn1 loop in the BS (Figure 2E). In particular, the number of contacts between the US and BS reaches nearly the same value at almost the same time after the elimination of the interactions between the PAR and DNA (orange shaded region), strongly suggesting that these specific contacts are critical for maintaining the closure of the Brn1 loop. Combined evidence from unbiased MD and steered MD simulations demonstrates that DNA entry stabilizes the closed conformation of the Brn1 loop. This mechanistic insight suggests that DNA-mediated loop stabilization can constitute a prerequisite for subsequent activation of SMC ATPase activity, ensuring the stability of the loop extrusion process.

Dynamics of DNA and Its Role in Modulating Safety-Belt Dynamics

AlphaFold predictions and all-atom MD simulations suggest that DNA entry into the Brn1 loop enhances the stability of the safety belt. However, these findings are confined to conformations near the closed crystal structure of the Brn1 loop, leaving the initial mechanism of DNA entry unresolved. Notably, our simulations indicate that the transition of the safety belt between the open and closed states is rarely observed within several microseconds in all-atom MD simulations (Figure S7), highlighting a limitation in capturing large-scale conformational transitions at atomic resolution. To overcome this problem and investigate the mechanism of DNA entrapment at spatio-temporal scales inaccessible with all-atom models, we developed a CG model of the Ycg1-Brn1-DNA complex. This model incorporates several key interaction terms to facilitate efficient exploration of the DNA capture process (Figure 3).

First, a sequence-independent interaction between DNA and Ycg1 is considered, which, in contrast to classical protein-DNA recognition, may enable condensin to access open chromatin regions, such as transcriptionally active genes or nucleosome-depleted sites [47, 48]. This non-specific interaction facilitates one-dimensional sliding of the complex along DNA and enables subsequent capture by the safety belt [49]. By ensuring the diffusion coefficients D are close in order of magnitude to the measured movement of cohesins and condensins moving diffusively along naked DNA *in vitro* (Figures 3A, S8 and S9) [50, 51, 52, 32, 53, 6, 54], and the DNA bending angle θ observed in the crystal structure is reproduced with a longer DNA sequence (Figure 3B) [21], we evaluated a range of interaction strengths between the Ycg1 HEAT-repeat subunit and DNA. The simulation closely matches experimental data in both D and θ , supporting the choice of $\varepsilon_{HD} = 0.6$ as the optimal interaction strength between DNA and Ycg1 (ε_{HD} is the scaling factor of the interaction strength between DNA and Ycg1, see Methods for details).

Second, the loop regions of Brn1 are largely unstructured, and the structured regions make few contacts with DNA, resulting in essentially no native contacts in the available structures. In our all-atom MD simulations with loop reconstruction, DNA interactions were primarily mediated by charged residues. Based on these observations, we focused on modeling Brn1-DNA interactions through electrostatics (Figure 3C).

Third, the strength of the interaction between the latch and the buckle (ε_{LB} , the scaling factor of the interaction strength between the latch and buckle) is challenging to determine, as there are no direct experimental data available. To avoid artifacts caused by an inappropriate choice of interaction strength, we systematically explored a range of

ε_{LB} values, allowing the transition of the safety belt from a fully open to a fully closed state during the simulation. To quantify the degree of closure, we calculated the order parameter Q , defined as the average fraction of native contacts formed with respect to the fully closed reference state [55]. Thus, a higher Q value indicates a conformation that is more similar to the closed structure (Figures 3D and 3E, see Methods for details).

Notably, this systematic tuning of ε_{LB} is not only a technical control to avoid simulation artifacts but also reflects potential biological modulation of the latch-buckle interface. We hypothesized that post-translational modifications such as phosphorylation within the latch and buckle, could effectively alter the local interaction strength *in vivo*. Given that condensin is regulated by phosphorylation in multiple organisms, with effects on loading and activity that implicate kleisin and HEAT subunits [56, 57, 58], we examined how phosphorylation could tune the opening and closure of the kleisin safety belt. Focusing on Brn1 sites in and around the latch-buckle region (including experimentally annotated positions such as S423 and S469), all-atom simulations with MM/GBSA analysis revealed site-specific shifts in latch-buckle affinity relative to wild type (Figure S10). Some phospho-variants weakened interfacial binding, whereas others strengthened it, and contact/electrostatic analyses rationalized the direction of change. In our CG framework these energetic shifts map naturally onto the latch-buckle interaction parameter ε_{LB} , providing a mechanistic route by which phosphorylation could bias safety-belt dynamics and, consequently, DNA capture [58]. This suggests clear experimental tests: phosphomimetic or phospho-null mutations at the identified sites should modulate the balance between opening (DNA outside the loop) and closure (DNA inside the loop).

Our simulations successfully recapitulated the complete process of DNA entrapment by the safety belt. To identify when DNA becomes truly encircled by the Brn1 loop, we calculated a topological linking number (see Methods for details). This allows us to distinguish the states when DNA is outside the loop (S_{nl} , “non-looped”) versus the ones when DNA is entrapped inside (S_l , “looped”, see Figure 4A). We then used Q between the latch and buckle to quantify the extent of safety-belt closure across trajectories. Compared to the DNA-free state (S_f), the Q value decreases in the S_{nl} , but increases in the S_l (Figure 4B). These results suggest that DNA can act bidirectionally: promoting opening when put outside the loop, and stabilizing closure upon entry. To further illustrate these findings, we provide a supplementary movie (Movie S1 and Figure S11) that directly visualizes how DNA binding influences the flexibility and dynamic behavior of the kleisin safety belt. This DNA-dependent stabilization is consistent with AlphaFold3 predictions and all-atom MD simulations. The observed trends are robust across a broad

range of ε_{LB} and ε_{HD} values (Figures 4B, S12 and S13). Notably, when the latch-buckle interaction becomes excessively strong (e.g., $\varepsilon_{LB} = 0.45$), the modulatory effect of DNA is largely abolished, likely due to saturation of the closure interface.

Interestingly, analysis of the DNA-Brn1 loop contacts reveals a compensatory mechanism: as ε_{LB} increases, a more stable loop conformation exposes additional DNA-binding sites, resulting in stronger interactions with DNA (Figure 4C). This is evident in the continuous increase in contact numbers in the S_{nl} , while the S_l shows only marginal changes. To dissect which interactions drive this behavior, we calculated the contact frequency between charged Brn1 residues and DNA phosphates (Figure S14). Our analysis shows that both S_{nl} and S_l are dominated by electrostatic interactions localized in basic Brn1 patches (residues 409-417 and 445-455), with R430 serving as a recurrent anchor; a further contact hotspot is seen near residue R480. These patches lie immediately adjacent to the latch-buckle closure path, so when DNA occupies them in the S_{nl} , phosphate-Lys/Arg engagement introduces both electrostatic attraction and steric interference that act to destabilize the latch-buckle interface. Consistent with this view, the difference in electrostatic contact frequency between S_{nl} and S_l increases with higher ε_{LB} , paralleling trends in Figure 4C. Together, these data support a mechanism in which DNA located outside the loop stabilizes S_{nl} by engaging basic Brn1 patches, thereby biasing the interface toward the open latch state. Intriguingly, this suggests that DNA, acting as a passive “passenger”, may guide its own entrapment by promoting tighter interactions when the safety belt approaches closure with electrostatic interactions appearing to provide the driving forces.

To further assess template dependence of our CG model, we compared protein-DNA contact maps from our CG simulation trajectories with those derived from the Ycg1-Brn1 crystal structure (PDB: 5OQO [22]) and from cryo-EM structures that contain longer DNA duplexes (PDB: 7QFW [15], PDB: 7Q2Z [21]). The simulations reproduce the core, high-occupancy contacts present in 5OQO and additionally form interactions that overlap with those in 7QFW and 7Q2Z, particularly at the Ycg1 N- and C-terminal regions (Figure S15). Although 7QFW and 7Q2Z reveal additional interfaces enabled by their longer DNA substrates, the anchoring contacts that define the interface are already captured by 5OQO, and our simulations recover the extended contacts as the DNA explores additional registers. These results indicate that our conclusions are not sensitive to the choice of initial template.

Effect of Latch-buckle Interaction Strength on the Kinetics of DNA Entrapment and Diffusion along DNA

Guided by the observation that DNA outside the Brn1 loop promotes opening while DNA inside the loop stabilizes closure, we next asked how the interaction strength between the latch and buckle (ε_{LB}) tunes the kinetics of DNA entrapment. We analyzed 50 independent CG MD simulation trajectories for each ε_{LB} value. Throughout the simulations, we identified four different states: (i) DNA unbound to the Ycg1-Brn1 complex (US), (ii) DNA interacts with the protein complex but located outside the Brn1 kleisin loop (IS_{out}), (iii) DNA surrounded by the Brn1 kleisin loop but with an unclosed latch-buckle interface (IS_{in}), and (iv) DNA fully entrapped by a closed loop (BS) (Figure 5A). The state classification was based on a combination of the Q , the number of contacts between DNA and the Ycg1-Brn1 complex, and the topological linking number (Figure S16). Note that IS_{out} is defined by the DNA path relative to the loop, not by latch geometry, so the latch can be either open or closed in IS_{out} .

We subsequently measured the mean first passage times for the transitions $US \rightarrow IS_{out}$, $IS_{out} \rightarrow IS_{in}$, $IS_{in} \rightarrow BS$, and the complete transition $US \rightarrow BS$ (Figures 5B and S17). Our results reveal that increasing ε_{LB} prolongs the transition from IS_{out} to IS_{in} , suggesting that stronger latch-buckle interactions hinder loop opening and thus delay DNA entry. Conversely, the transition from IS_{in} to BS becomes markedly faster with increasing ε_{LB} , reflecting facilitated loop closure once DNA is in place. The opposing influences of these two steps result in a non-monotonic transition time dependence of the process from US to BS under different ε_{LB} , which initially decreases and subsequently increases. The D has been shown to influence condensin in locating appropriate anchoring sites and promoting linear compaction of chromatin [54]. Motivated by this, we hypothesized that the stability of the safety-belt structure might similarly regulate the diffusion of DNA. To test this idea, we measured the one-dimensional diffusion rate of the safety belt (essentially, the diffusivity of the condensin complex along DNA) as a function of latch-buckle interaction strength. Our results revealed a clear inverse correlation: stronger interactions between the latch and buckle significantly slowed the diffusion of the safety belt on DNA (Figures 5C and S18).

A schematic free energy landscape illustrating these kinetic trends is shown in Figure 5D. Mechanistically, enhanced latch-buckle interactions impede DNA surrounded by the Brn1 loop ($IS_{out} \rightarrow IS_{in}$), but promote rapid closure of the Brn1 loop once DNA has entered ($IS_{in} \rightarrow BS$). From a functional standpoint, strengthening ε_{LB} increases the stability of the fully engaged BS state, which in turn can facilitate the hydrolysis of ATP by the SMC2-SMC4 AT-

Pase domains [22]. However, if ε_{LB} becomes too strong, the energetic barrier of DNA entrapment by Brn1 loop becomes prohibitively high, compromising the efficiency of DNA capture. Together, these findings suggest that an optimal latch-buckle interaction strength must balance structural stability with accessibility. Moreover, the strength of the safety belt can also regulate DNA diffusion during the process of loop extrusion, thereby assisting condensin in locating appropriate anchoring sites and facilitating linear compaction of the chromatin [54, 9]. The observed phenomena remain robust over a wide range of CG modelling parameters, underlining the generality of the mechanism (Figure S19).

Discussion

Using an integrated multiscale computational strategy combining AlphaFold3 predictions with all-atom and CG MD simulations, our study reveals that DNA is not just a passive participant but an active regulator of Sc condensin's safety-belt dynamics: it triggers the "latch" to open or close at appropriate times to support efficient loop extrusion. In the presence of DNA, the safety-belt interface is markedly stabilized, consistent with a state primed for ATP hydrolysis and loop extrusion. While in the absence of DNA, the belt is more flexible, presumably to allow initial DNA entry. Our results identify how DNA binding reduces the mobility of the flexible segment of the safety belt, stabilizes latch-buckle contacts, and biases opening events depending on whether DNA is positioned outside or captured inside the loop. These local mechanical effects provide a concrete rationale for the DNA-stimulated steps that precede head engagement and loop growth seen in single-molecule assays of condensin and cohesin [10, 32, 11].

AlphaFold3 has demonstrated remarkable success in predicting static protein structures [38]. However, it remains an open question to what extent it captures protein dynamics. Recent studies have shown that it can implicitly learn key aspects of protein conformational variability [59, 39, 43, 44, 40]. Motivated by these insights, we quantified an effective strain from the AlphaFold PAE matrices to compare the Brn1 loop in the US and BS. Consistently lower PAE-derived strain in BS indicates reduced local flexibility upon DNA entry, a trend that we independently reproduced with all-atom and CG MD simulations, lending support to the idea that AlphaFold predictions with appropriate interpretation can be used to inform the conformational flexibility [38, 59, 39, 43, 44, 40].

To capture the large-scale dynamics of DNA entry into the safety belt, we employed CG simulations that successfully observed the entire DNA entrapment process. The simulations revealed that DNA has distinct guiding

roles during this process: when DNA is located outside the Brn1 loop, it facilitates loop opening, whereas once DNA is inside the loop, it promotes loop closure (Figure 4B). Accordingly, four key states were identified along the pathway: US, IS_{out}, IS_{in} and BS (Figure 5A). The intrinsic flexibility of the kleisin linker allows conformational rearrangements that transiently expose the positively charged DNA-binding groove formed by the Ycg1-Brn1 complex, enabling DNA to associate through non-topological interactions in the IS_{out} state. Because these contacts are not topologically constrained, they are expected to be structurally unstable and readily disrupted by experimental perturbations such as mechanical stress or electrophoretic conditions. Together, these results suggest that, beyond its role in topological entrapment, the safety belt may also modulate transient non-topological DNA interactions through its conformational flexibility, providing structural insight into intermediate states along the condensin loading pathway.

Electrostatics emerge as the primary driver of DNA positioning. Even when we remove the explicit short-range Ycg1-DNA attraction ($\varepsilon_{HD} = 0$), DNA still accumulates near the positively charged binding groove (Figure S14). This indicates that long-range electrostatic attraction to basic patches on Brn1 is sufficient to form an encounter complex; increasing ε_{HD} then deepens and stabilizes this pre-bound state but is not required to create it. This behavior is consistent with earlier blind CG predictions that omitted a full Brn1 description yet nonetheless recovered electrostatically guided DNA placement near the groove [60]. However, purely electrostatic interactions between DNA and the condensin complex are insufficient to explain several key experimental observations. For example, condensin's diffusion along DNA and the local DNA bending induced by the safety belt cannot be accounted for by long-range electrostatics alone [21, 54]. Therefore, introducing additional non-covalent interactions between DNA and the safety belt is essential for a more realistic and functional model. Given that condensin captures DNA through sequence-independent binding [22], we developed a modified Gō-like interaction potential that enables sequence-unspecific DNA recognition, supports one-dimensional diffusion consistent with the measured diffusive movement of cohesins and condensins along naked DNA *in vitro*, and accurately reproduces local DNA bending observed in crystal structures (Figures 3A and 3B). By tuning parameters within biologically relevant ranges, our model closely matches experimental behavior. Remarkably, at near-physiological protein concentrations, we observed the safety belt sliding along DNA, consistent with previous *in vitro* findings [10]. This semi-diffusive sliding may facilitate chromosome folding by allowing condensin to explore local DNA configurations. Additionally, this sliding suggests that short or linear DNA fragments, unable to be

topologically trapped, may escape the safety belt through diffusion in a native-like configuration in experiments.

We found a clear monotonic relationship between the stability of the safety belt and the degree of DNA sliding, suggesting a potential role in controlling its movement. Meanwhile, our simulations suggest that excessive sliding speed can disrupt stable DNA entrapment, impairing safety-belt closure (Figure S13). This delicate balance between mobility and stability may act as a key regulatory mechanism in condensin's function during chromosomal loop extrusion. Interestingly, although yeast condensin is considered an asymmetric and unidirectional loop extruder-reeling in DNA loops from only one side-experiments have shown that it transitions from a static to a sliding behavior under near-physiological ionic conditions [10]. Although salt concentration was not explicitly investigated, our results imply that it may influence DNA-protein interactions, which are mostly electrostatic, and consequently, the sliding behavior of DNA, which could play a role in regulating safety-belt opening and closure. Furthermore, our condensin-focused CG framework aligns with established protein-DNA CG practices: it shares the interaction ingredients that have enabled accurate replisome-histone recycling [61], chaperone-assisted H2A/H2B eviction [62], mismatch-repair MutS sliding [63], and translocase-driven nucleosome repositioning [64]. This broader context underscores the validity and robustness of CG approaches for studying long-timescale protein-DNA dynamics [65].

We demonstrate how multiscale simulation can extend static Ycg1-Brn1 structures into a dynamic framework for DNA capture. AlphaFold-based analyses and all-atom MD localize the residues that change flexibility and interaction energy upon DNA binding, while CG simulations access long-timescale opening and closing of the kleisin loop and allow controlled tests of DNA topology. This division of labor follows a good practice for protein-DNA systems in which flexible and partly unstructured segments drive function [65]: atomistic model to validate the interfaces, CG model to study the kinetics and routes for protein-DNA binding. Together, these scales reveal where DNA stabilizes the loop, how latch-buckle contacts reorganize, and when DNA positioning biases the system toward closure.

CG models exchange atomic detail and absolute kinetic fidelity for access to longer timescales and larger conformational changes. They are therefore most reliable for mechanistic trends rather than precise rate constants [66, 67]. In this spirit, our conclusions emphasize (i) relative stabilization of the latch upon DNA entry, (ii) redistribution of DNA-protein contacts, and (iii) topology-dependent gating of capture, all robust across parameter ranges. Several extensions could sharpen mechanism and bridge further to experiment. First, incorpo-

rating sequence-dependent DNA mechanics/electrostatics and explicit hydrodynamic interactions should improve the realism of diffusion and capture in CG models [67, 68]. Second, adding the SMC head/ATPase modules would link latch dynamics directly to the nucleotide cycle; doing so at scale will likely require hybrid all-atom/CG strategies and/or enhanced sampling [69, 70]. Third, targeted experiments can test our predictions: mutating latch/buckle residues highlighted by effective-strain and MM/GBSA analyses; single-molecule FRET or optical/magnetic tweezers to resolve DNA-outside versus DNA-inside states and latch opening/closure; and cryo-EM aimed at intermediates captured along the path to entrapment. Finally, our model predicts a kinetic trade-off: weakening latch-buckle cohesion should accelerate initial capture but reduce retention on DNA, whereas strengthening should slow capture but stabilize engagement. These effects can be assayed by interface mutations while measuring loop-extrusion rates and dwell times *in vitro*.

Our study offers significant mechanistic insights, yet several questions remain. For example, the energetic contributions of specific residue interactions within the Brn1 loop and potential allosteric effects on other SMC subunits require further exploration. Recent studies have extended similar modeling approaches to larger systems containing multiple SMC subunits, offering important insights into the cooperative and potentially synergistic behavior of SMC complexes in loop extrusion [71]. Although constructing a complete SMC complex to directly visualize this process remains a substantial challenge, our model could, in principle, be further scaled to such multi-subunit systems in the future to explore these collective mechanisms in greater detail. Recent evidence highlights asymmetric DNA loop extrusion as a shared mechanism among eukaryotic SMC complexes, supported by single-molecule and structural studies of condensin, cohesin, and SMC5/6 [9]. Notably, a safety-belt-like structure has been identified in the Scc3-Scc1 subcomplex of the budding yeast cohesin complex [33], suggesting that, despite variations in composition and regulation across species, asymmetric loop extrusion may be a conserved feature of SMC complexes. Extending our model to other SMC complexes could reveal whether DNA-mediated safety-belt regulation is a universal mechanism in SMC-mediated chromosome organization.

DNA stimulates condensin's ATPase and motor activity *in vitro* [72, 24, 73, 74], and recent cryo-EM has revealed ATP-engaged, DNA-clamped states at the SMC head module [8, 21, 15, 14, 75]. What remains unresolved is the allosteric pathway linking DNA capture at the kleisin safety belt to head engagement and ATP turnover, which motivates simulations that explicitly include the head module in defined nucleotide states. While fully explicit simulations of the SMC head ATPase cycle requires hybrid

QM/MM treatments of phosphoryl transfer and extensive sampling of nucleotide-coupled head engagement [76, 77], thus remain out of scope, the available cryo-EM templates make a staged multiscale strategy feasible. One would first parameterize the head modules in defined nucleotide states from cryo-EM and couple these head states to the DNA-dependent safety-belt states mapped here. Then allosteric pathways between the safety belt and the heads can be simulated using enhanced sampling or hybrid all-atom/CG models, while reserving focused QM/MM calculations only for the catalytic pocket during ATP hydrolysis [76, 77]. In this context, our results here supply the upstream, DNA-dependent stabilization that is expected to bias head engagement, offering testable predictions for how latch mutations or DNA topology should modulate DNA-stimulated ATPase activity.

Although we focus on budding-yeast condensin, the principles we uncover are general. DNA entrapment within kleisin-defined gates and regulation of loop opening via latch stability map onto conserved SMC features; cohesin clearly extrudes loops, and related gate-and-clamp architectures are shared across the SMC family [78]. Mechanistically, we find that DNA actively steers the safety belt: DNA positioned outside the Brn1 loop biases the latch toward opening, whereas DNA inside the loop stabilizes latch-buckle closure. The effective strength of the latch-buckle interaction sets a trade-off between capture (entry) and retention (closure), providing a simple control knob for loop-extrusion efficiency. Because SMC complexes organize genome folding, replication, and gene regulation, linking DNA capture and latch stabilization to loop control has broad implications. In particular, SMC dysfunction is frequent in human cancers and associated with transcriptional dysregulation and chromatin reorganization [36, 35], suggesting that perturbations to kleisin-gate mechanics by mutation or post-translational modification, could propagate to chromosome-scale architecture. Our multiscale strategy, which is AlphaFold3-guided modeling integrated with all-atom and CG MD simulations, provides a transferable way to quantify effective strain, contact dynamics, and loop flexibility in protein-DNA complex. The resulting picture is a unified, testable model in which DNA modulates the kinetics and stability of the kleisin safety belt through electrostatic and latch-buckle interactions. We anticipate that the same design framework can be applied across SMC families and further be extended to larger assemblies to connect protein-DNA gate mechanics with ATP-cycle control and long-range genome organization.

Methods

PAE-Predicted Effective Strain

AlphaFold provides confidence-derived outputs that are informative about conformational variability, in addition to static structural models [43, 42, 39, 40]. We quantify local deformation with the residue-wise metric ES_i , designed to sensitively report changes in local structure. Operationally, ES_i summarizes the mean relative change in inter-residue PAE values around residue i (formal definitions below); the pairwise quantity ES_{ij} analogously tracks changes for a specific residue-partner pair. The PAE is provided by AlphaFold for every residue pair and reports the expected positional error (in Å) at residue i if the predicted and true structures were aligned on residue j . Low PAE indicates high confidence in the relative placement of segments (e.g., domains), whereas high PAE indicates uncertainty consistent with flexible or variably oriented regions. Previous work shows that patterns in PAE correlate with MD markers of motion (e.g., distance-variation matrices), supporting the use of PAE as a reasonable proxy for conformational heterogeneity [41]. Community tools routinely use PAE to identify mobile domains and hinges and to parse domain groupings in predicted models. On this basis, we use ES_i and ES_{ij} to summarize changes in local PAE within and across states; we emphasize that PAE is a confidence-based surrogate rather than a direct kinetic observable and therefore corroborate PAE-based trends with MD simulations.

For each residue i , we define a neighborhood set $\|N_i\|$ comprising n_i number of residues $j \in \|N_i\|$ with $C\alpha$ distances r_{ij} within 13 Å. Here, the calculation only involved the residues with AlphaFold3 predicted pLDDT > 70 , which is a commonly used threshold indicating at least correct backbone geometry [43, 44]. For each state (US and BS), we generated 10 independent AlphaFold3 predictions. Predicted models were compared to the corresponding experimental structures (US: PDB 5OQQ; BS: PDB 5OQO) by computing backbone $C\alpha$ RMSD after superposition on protein $C\alpha$ atoms; DNA atoms were excluded from the alignment. Summary statistics are reported in Table S2. The ES_i is the average of ES_{ij} over the N_i neighbors:

$$ES_i = \frac{1}{n_i} \sum_{j=1}^{n_i} ES_{ij} = \frac{1}{n_i} \sum_{j=1}^{n_i} \frac{PAE_{ij}}{r_{ij}}. \quad (1)$$

The ES_i is defined for a single predicted structure, representing the average of different ES_{ij} , whereas $\langle ES_i \rangle$ denotes the average of ES_i values across 10 independent structures, providing a measure of the residue's consistency and reliability over multiple predictions. If $n_i = 0$ (i.e., no neighbors of residue i), $\langle ES_i \rangle$ was deemed undefined, thus not plotted. In addition to Figure 1C and 1D,

which highlights the Brn1 residues 383-423 window most relevant to safety-belt opening, a belt-wide $\langle ES_i \rangle$ profile and the full $\langle ES_{ij} \rangle$ matrix (Brn1 residues 383-524) are reported in the Supplementary Information for reference (Figure S3).

To assess whether PAE-derived effective strain captures local sensitivity to perturbations in the latch region, we modeled four mutations with reported latch-buckle weakening effects (M391D, F394D, W402D, W408D) and compared wild-type and mutant ensembles [22]. For each variant we calculated

$$\Delta \langle ES_i \rangle = \langle ES_i^{\text{Mut}} \rangle - \langle ES_i^{\text{WT}} \rangle \quad (2)$$

and summarized the local response by aggregating $\Delta \langle ES_i \rangle$ within radial shells of 13, 15, and 18 Å centered on the mutated residue (Figure S1). This shell-based analysis follows recent work relating AlphaFold-predicted local deformation to experimental mutational effects [43, 44]. Full calculation details are provided in the Supplementary information.

All-atom MD Simulations

The initial structure of all-atom MD simulation was constructed based on the crystal structure (PDB code: 5OQQ) [22]. Missing residues in the crystal structure were reconstructed using Modeller 10.4 [79]. The DNA-free structure was obtained by removing the DNA from the reconstructed structure. All systems were built using the web-based CHARMM-GUI Membrane Builder [80]. CHARMM36m force field was used to describe the interactions [81]. The steered MD was conducted to compare the impact of the Brn1 loop encircling DNA on the safety belt. A single reaction coordinate was defined between two groups, the first N-terminal $C\alpha$ atom of the latch region in the Brn1 loop (the pulling group) and the Ycg1 (the reference group). An external harmonic potential was applied along the z-axis using the "direction" geometry, with pulling dimensions set to only affect the z-coordinate (Figure S6). The pulling was performed at a constant rate of 0.005 nm ps⁻¹, with a force constant of 600 kJ mol⁻¹ nm⁻². The initial distance between the COMs of the two groups was used as a starting point, and the periodic boundary conditions were accounted for by updating the reference coordinates at each step. The protein placed in the center of the box and is rotated in a way that the DNA binding groove is located in the direction of the z-axis. The atom positions of the protein with $z < 14$ nm in our box are fixed to ensure that the position of the Ycg1 HEAT-repeat does not change, and the remaining parts are not fixed to keep the binding position as flexible as possible (Figure S6). The steered MD runs of 2500 ps fully extract the latch region from the buckle region.

Unbiased MD and steered MD simulations were conducted using the GROMACS 2022.5 package with an integration time step of 2 fs [82]. Coulomb interactions were shifted to zero between 1.0 and 1.2 nm, and a cutoff radius of 1.2 nm was applied for Lennard-Jones interactions. The system temperature was maintained at 310 K using a velocity-rescaling thermostat, and the pressure was kept at 1 bar in all directions with a Parrinello-Rahman barostat. Simulation boxes was set to $17 \times 17 \times 17 \text{ nm}^3$, which was filled with TIP3P water molecules, and 0.15 M NaCl was added to mimic the physiological conditions. We performed three independent unbiased MD simulations for each system, each running for 1 μs .

CG MD simulations of Ycg1-Brn1 in Complex with DNA

To investigate the large-scale dynamics of DNA entering the safety belt, we employed CG MD simulations. For the Ycg1-Brn1 complex, a residue-level CG model (AICG2+) was used [83, 84, 85], with each bead positioned at the $\text{C}\alpha$ atom location and interactions only including those appearing in the native crystal structure (PDB: 5OQO) [22]. Considering the lack of structural information for the unstructured region (residues 413-456) in Brn1, we removed the native contact potentials and retained only the generic local potentials derived from a “loop-segment library” based on Protein Data Bank statistics to better capture its dynamic behavior. These generic local potentials effectively describe the conformational distribution of unfolded states or intrinsically disordered regions by accounting for secondary structure propensities [86]. Complete CG model parameters and Ycg1-Brn1 simulation settings are provided in the Supplementary information. For DNA, we employed the 3SPN.2C model [87], which captures base-pairing, hybridization, groove widths, and local curvature. In this model, each nucleotide is represented by three beads corresponding to the phosphate, sugar, and base groups. To prevent the false capture of DNA, where one end of short linear DNA fragments may pass through the safety belt, we extended the original 18-bp DNA double helix by 40 bp at each end, resulting in a 98-bp DNA double helix structure. A spherical flat-bottom potential, with a radius of 10 nm, was applied between the COMs of the original 18-bp DNA residues and the protein center. No periodic boundary conditions were used in any direction in CG MD simulations.

The Ycg1-Brn1 complex and DNA interact through long-range electrostatics, excluded volume, and a non-specific interaction of the protein-DNA sequence, which expands the $\text{G}\ddot{\text{o}}$ -like potential for the Ycg1-DNA interaction observed in the crystal structure. Similar simulation setups have proven broadly applicable and effective in modeling protein-DNA systems [64, 62, 61, 63, 88, 65].

We first extract the native contact list between Ycg1 and DNA. These interactions were formed between a set of protein residues and related phosphate or sugar beads of DNA in the crystal structure. We then expanded this list by modifying the index of phosphate and sugar in DNA to cover the entire 98-bp range of DNA.

To determine the interaction strength between the DNA duplex and Ycg1 (the scaling factor ε_{HD} from the default values in the original CG model), we first compared the mean experimentally accessible value of the D for cohesins and condensins diffusing along naked DNA. The experimentally measured range of D value *in vitro* is approximately from 0.01 to 35 kb^2/s [54]. When $\varepsilon_{\text{HD}} \geq 0.5$, the simulated diffusion coefficient D reaches values ranging from several tens to over a hundred kb^2/s , approaching the upper bound of *in vitro* experimental measurements. Given that CG simulations generally overestimate diffusion due to reduced frictional damping [89], this level of agreement is remarkably close to experimental observations. Notably, when $\varepsilon_{\text{LB}} \leq 0.6$, the DNA bending angle (θ) observed in the simulations aligns well with that seen in crystal structures with a longer DNA fragment (PDB: 7Q2Z) [21]. By comparing the D and θ at different interaction strengths with the angle in the crystal structure, we determined that the interaction strength scaling factor (ε_{HD}) is 0.6. Separately, to validate our choice of the 5OQO structure as a starting model, we performed a comparative analysis of protein-DNA contacts. This analysis confirms that our simulation successfully recapitulates the primary DNA contact map observed in more physiologically relevant cryo-EM structures with longer DNA substrates (Figure S15). Additionally, we focused on the impact of the interaction strength between the latch and the buckle (the scaling factor ε_{LB} from the default values in the original CG model) in the safety-belt model on the overall dynamics of DNA entry. To explore this, we tested a range of ε_{LB} with varying interaction strengths, specifically between 0.3 and 0.5, performing 10 independent simulations for each parameter. Each simulation system was run for a total of 100 μs . The probability distribution of Q under these parameters is shown in Figure 3D. Our results demonstrate that the interaction strength between latch and buckle produces a shift in the mean value of Q from approximately 0 to 1 (Figure 3E), indicating that the safety belt can transition from almost fully open to fully closed under the tested conditions.

Our all-atom MD simulations reveal that the interaction between DNA and Brn1 is primarily electrostatic near the crystal structure (Figure 3C). Considering that there are only a few amino acid residues on Brn1 kleisin that have native contact with DNA in the crystal structure, and these residues are predominantly charged, we focus on electrostatic interactions and volume repulsion between DNA and Brn1 without adding additional $\text{G}\ddot{\text{o}}$ -like poten-

tial. Following the suggested parameters [90, 87], we assigned a charge of -0.6e to each phosphate bead for DNA-DNA electrostatic interactions, ensuring the appropriate DNA persistence length and accounting for the Oosawa-Manning condensation of counterions surrounding DNA. For Ycg1-Brn1-DNA electrostatics, we set the phosphate charges to -1e, as described previously [91, 92]. Electrostatics is modeled according to the Debye-Hückel theory. Notably, similar CG models have been used for studying diverse protein-DNA dynamics, including parental H3/H4 recycling at replication forks [61], Nap1-mediated H2A/H2B eviction from partially unwrapped nucleosomes [62], MutS sliding along DNA during mismatch recognition [63], and nucleosome repositioning via lane-switching driven by DNA translocases [64]. These precedents support the generality of CG force-field components we used here.

All CG MD simulations were performed using GENESIS (version 2.1.2) with an integration time step of 0.01 ps [93]. Langevin dynamics with default parameters were employed at a temperature of 310 K. To investigate the kinetics of DNA entry under different conditions, 50 independent 10 μ s simulations were conducted for each condition. A summary of the simulation systems and durations is provided in Table S3. The total simulation time for the Ycg1-Brn1-DNA complex system was 6700 μ s, while for the Ycg1-Brn1 complex system it was 600 μ s. The ionic strength was set to 0.15 M.

Data Analysis

Visualization of the structures was performed with Visual Molecular Dynamics (VMD, version 1.9.4) [94] and PyMOL (version 0.99) [95] software. The GROMACS built-in tools were used to analyze MD trajectories. To examine how the presence of DNA affects the stability of the safety belt in all-atom MD simulations, “*gmx_mindist*” was adopted with a cutoff distance of 0.6 nm to calculate the contact number. The interactions between the DNA and protein residues were described by the normalized number of contacts, which is defined by the ratio of the average number of contacts per frame of each residue to the maximum calculated above. RMSF was calculated with “*gmx_rmsf*”. The fraction of native contacts Q formed by the latch and buckle in the crystal structure is determined by the switching function:

$$Q = \frac{1}{N_{nc}} \sum_{i,j} \frac{1}{1 + \exp(\beta(r_{ij} - \lambda r_{ij}^0))}, \quad (3)$$

where N_{nc} is the number of native contacts, r_{ij}^0 is the distance between C α atoms of residues i and j forming native contacts in the crystal structure, and parameters $\lambda = 1.5$, $\beta = 50, \text{nm}^{-1}$ control the slope of the switching

function. The calculation of probability distribution of Q was carried out with the aid of the PLUMED plugin (version 2.9.0) [96, 97].

To quantify the one-dimensional diffusion of the condensin along DNA, we calculated the mean square displacement (MSD) based on the index of the DNA base pair nearest to the binding site at each frame. Specifically, the MSD was computed as:

$$\text{MSD}(n, N) = \frac{\sum_{k=1}^{N-n} (\text{bp}_{k+n} - \text{bp}_k)^2}{N - n}, \quad (4)$$

where bp_k denotes the base pair index closest to the protein binding site at frame k , N is the total number of frames in the trajectory, n is the frame lag, and Δt is the time interval between two consecutive position measurements. Although this coordinate system is discrete, it captures the stepwise transitions of the protein binding site along the DNA sequence and is suitable for analyzing sliding or hopping behavior [98].

To estimate the diffusion coefficient D , we focused on the initial linear regime of the MSD curve, where MSD increases approximately linearly with lag time:

$$\text{MSD}(n, N) = 2D n \Delta t. \quad (5)$$

To ensure reliable fitting and minimize statistical uncertainty, we imposed a cutoff lag n_c , chosen so that the relative error in MSD remained below 20% [99, 98]. The MSD variance was estimated as:

$$\sigma^2(n, N) = \frac{(2Dn\Delta t)^2(2n^2 + 1)}{3n(N - n + 1)}, \quad (6)$$

so that the cutoff was determined by satisfying:

$$\frac{\sigma(n, N)}{2Dn\Delta t} < 0.2. \quad (7)$$

To minimize potential artifacts in the MSD analysis introduced by the flat-bottom potential (10 nm radius) between the COMs of the original 18-bp DNA residues and the protein complex, we excluded trajectory segments where the protein approached the ends of the DNA duplex. The DNA molecule spans 98 base pairs, with an average spacing of 0.34 nm per base pair. Thus, the central region of approximately 58 base pairs corresponds to a 20 nm potential-free zone (diameter, calculated as 10 nm radius \times 2). To avoid edge effects, we only analyzed trajectory segments where the DNA base pair closest to the protein binding site continuously resided within the central 50 base pairs (well within the ~58 bp potential-free zone) for at least 1000 frames (100 ns). Based on this criterion, the number of valid trajectory segments obtained under different ε_{HD} was 3 ($\varepsilon_{HD} = 0$), 182 ($\varepsilon_{HD} = 0.3$), 75 ($\varepsilon_{HD} = 0.5$), 54 ($\varepsilon_{HD} = 0.6$), 32 ($\varepsilon_{HD} = 0.7$), 55 ($\varepsilon_{HD} = 0.9$), and 11 ($\varepsilon_{HD} = 1$). For the latch-buckle interaction strength (ε_{LB}),

due to the availability of more extensive trajectories, we applied a stricter criterion, requiring the closest base pair to remain within the central 50 base pairs for at least 5000 frames (500 ns). The resulting numbers of valid trajectory segments were: 114 ($\varepsilon_{LB} = 0.3$), 116 ($\varepsilon_{LB} = 0.35$), 108 ($\varepsilon_{LB} = 0.37$), 121 ($\varepsilon_{LB} = 0.4$), and 109 ($\varepsilon_{LB} = 0.45$).

Under our simulation conditions, we selected $n_c \approx 60$ frames (6 ns) for segments of 1000 frames (100 ns) and $n_c \approx 300$ frames (30 ns) for segments of 5000 frames (500 ns). This choice balances statistical accuracy and time resolution and ensures that the estimated D reflects genuine sequence-position dynamics.

We calculated the average DNA bending angle (θ) from the CG MD trajectories using MDAnalysis [100]. Only frames that met both $Q \geq 0.8$ and linking number ≥ 0.8 (i.e., the BS state) were used for bending analysis. For each such frame, we constructed the DNA central axis as follows: first we located a dynamic pivot—the DNA base atom (named “DB”) closest to the COMs of key residues on Ycg1 (residue indices 240, 241, 242, 243, 245, 246, 247), which define its primary DNA binding site. Then, using symmetric windows of approximately 31 base pairs upstream and 13 base pairs downstream from that pivot, we computed geometric centroids of complementary DB atom pairs to approximate the double-helix axis. To quantify bending in each frame, we used a sliding-window approach along this axis: for each point, one vector was drawn to the centroid of the three preceding points, and another to the centroid of the three following points. The smallest angle between any such vector pair over all points was taken as the bending angle θ for that frame; smaller angles correspond to sharper bends. We repeated this for all valid frames across 10 independent simulation replicas. The mean bending angle for each system was then obtained by averaging across trajectory angle time series, and the standard error of the mean (SEM) was estimated from the replicate averages.

The number of contacts between two specified groups in the CG MD simulations was calculated using the “COORDINATION” collective variable implemented in PLUMED plugin [96]. This collective variable computes a smooth coordination number, defined as a differentiable sum over all pairs of CG beads $i \in A$ and $j \in B$:

$$C = \sum_{i \in A} \sum_{j \in B} s(r_{ij}), \quad (8)$$

where r_{ij} is the distance between beads i and j , and

$$s(r_{ij}) = \frac{1 - \left(\frac{r_{ij}}{r_0}\right)^n}{1 - \left(\frac{r_{ij}}{r_0}\right)^m} \quad (9)$$

is a switching (or rational) function that smoothly interpolates between 1 for $r_{ij} \ll r_0$ and 0 for $r_{ij} \gg r_0$, avoiding discontinuities in derivative. According to PLUMED

documentation, by default $n = 6$ and $m = 12$, producing a sharp but continuous transition around r_0 [96]. In our implementation, we set $r_0 = 0.8$ nm, while $n = 6$ and $m = 12$ remained at the default values. This configuration gives a smooth counting function: bead pairs much closer than r_0 contribute values close to 1 to the sum, while bead-pairs significantly farther contribute values near 0. This ensures that the coordination number reflects nearby contacts without abrupt cutoffs.

The topological state between the Brn1 loop and DNA was quantified using the concept of “linking number”, a fundamental invariant in knot theory that measures the entanglement of two closed curves in three-dimensional space [101]. For two non-intersecting closed curves γ_1 and γ_2 , the linking number $\Phi(\gamma_1, \gamma_2)$, defined via the Gauss linking integral,

$$\Phi(\gamma_1, \gamma_2) = \frac{1}{4\pi} \oint_{\gamma_1} \oint_{\gamma_2} \frac{\mathbf{r}_1 - \mathbf{r}_2}{|\mathbf{r}_1 - \mathbf{r}_2|^3} \cdot (d\mathbf{r}_1 \times d\mathbf{r}_2). \quad (10)$$

is an integer that remains invariant under continuous deformations, representing the number of times one curve winds around the other. Here \mathbf{r}_1 and \mathbf{r}_2 are the position vectors of points in the curve γ_1 and γ_2 , respectively. In our MD system, we modeled the Brn1 loop as a closed curve by connecting its termini with a straight line. This approximation is physically reasonable, as it captures the effective linking when the DNA is entangled by the Brn1 loop and the auxiliary segment. To treat the finite-length DNA duplex as a topologically closed curve, we extended the nearly linear DNA infinitely from its termini along the axial direction. Because contributions to the linking integral from distant segments are negligible, we truncated the extension beyond 4 nm from each terminus. The resulting DNA segment is sufficiently long relative to the Brn1 loop to effectively approximate an infinite-length DNA. The linking number between the Brn1 loop and the extended DNA segment was computed numerically. Convergence tests confirmed that extending the DNA beyond 106 nm did not alter the integral value, indicating a stable topological classification. Instances where the extended DNA overlapped with the Brn1 loop (resulting in non-integer values due to numerical singularities) were rare and excluded from analysis. The computed linking number was strictly quantized: $\Phi(\gamma_1, \gamma_2) = 0$ indicated that the DNA duplex was located outside the loop without threading, whereas $|\Phi(\gamma_1, \gamma_2)| = 1$ indicated that the DNA duplex passed through the Brn1 loop. This approach provided a robust metric to statistically resolve DNA-loop threading events in our simulations.

Data availability

All the processed data are presented in the main article and the Supplementary Information. Source data are

provided in the Source data file. Necessary files for setting up all-atom and CG MD simulations, as well as the AlphaFold3 predicted structural data generated in this study, are publicly available on Zenodo at <https://doi.org/10.5281/zenodo.17637587>. Protein sequences used for structure prediction were retrieved from UniProtKB under accession codes Q06680 (Ycg1) [<https://www.uniprot.org/uniprotkb/Q06680>] and P38170 (Brn1) [<https://www.uniprot.org/uniprotkb/P38170>]. The DNA sequence used for prediction was derived from Protein Data Bank (PDB) entry 5OQO [<https://doi.org/10.2210/pdb5OQO/pdb>]. Previously published protein structures used in this study are available in the PDB under accession codes 5OQO [<https://doi.org/10.2210/pdb5OQO/pdb>], 7QFW [<https://doi.org/10.2210/pdb7QFW/pdb>], and 7Q2Z [<https://doi.org/10.2210/pdb7Q2Z/pdb>].

Code availability

Scripts and code used in this paper have been deposited in Github under accession <https://github.com/JChen901/SafetyBeltData> and a backup of this repository is available via <https://doi.org/10.5281/zenodo.17637587>.

References

- [1] C.A. Martin, J.E. Murray, P. Carroll, A. Leitch, K.J. Mackenzie, M. Halachev, A.E. Fetit, C. Keith, L.S. Bicknell, A. Fluteau et al. Mutations in genes encoding condensin complex proteins cause microcephaly through decatenation failure at mitosis, *Genes Dev.* **30**, 2158 (2016)
- [2] R.E. Phillips, A.A. Soshnev, C.D. Allis. Epigenomic reprogramming as a driver of malignant glioma, *Cancer cell* **38**, 647 (2020)
- [3] H.K. Norton, J.E. Phillips-Cremins. Crossed wires: 3d genome misfolding in human disease, *J. Cell Biol.* **216**, 3441 (2017)
- [4] F. Uhlmann. Smc complexes: from dna to chromosomes, *Nat. Rev. Mol. Cell Biol.* **17**, 399 (2016)
- [5] K. Jeppsson, T. Kanno, K. Shirahige, C. Sjögren. The maintenance of chromosome structure: positioning and functioning of smc complexes, *Nat. Rev. Mol. Cell Biol.* **15**, 601 (2014)
- [6] T. Terakawa, S. Bisht, J.M. Eeftens, C. Dekker, C.H. Haering, E.C. Greene. The condensin complex is a mechanochemical motor that translocates along dna, *Science* **358**, 672 (2017)
- [7] T. Hirano. Condensin-based chromosome organization from bacteria to vertebrates, *Cell* **164**, 847 (2016)
- [8] B.G. Lee, F. Merkel, M. Allegretti, M. Hassler, C. Cawood, L. Lecomte, F.J. O'Reilly, L.R. Sinn, P. Gutierrez-Escribano, M. Kschonsak et al. Cryo-em structures of holo condensin reveal a subunit flip-flop mechanism, *Nat. Struct. Mol. Biol.* **27**, 743 (2020)
- [9] R. Barth, I.F. Davidson, J. van der Torre, M. Taschner, S. Gruber, J.M. Peters, C. Dekker. SMC motor proteins extrude dna asymmetrically and can switch directions, *Cell* **188**, 749 (2025)
- [10] M. Ganji, I.A. Shaltiel, S. Bisht, E. Kim, A. Kalichava, C.H. Haering, C. Dekker. Real-time imaging of dna loop extrusion by condensin, *Science* **360**, 102 (2018)
- [11] I.F. Davidson, B. Bauer, D. Goetz, W. Tang, G. Wutz, J.M. Peters. Dna loop extrusion by human cohesin, *Science* **366**, 1338 (2019)
- [12] I.F. Davidson, J.M. Peters. Genome folding through loop extrusion by smc complexes, *Nat. Rev. Mol. Cell Biol.* **22**, 445 (2021)
- [13] C. Arnould, V. Rocher, A.L. Finoux, T. Clouaire, K. Li, F. Zhou, P. Caron, P.E. Mangeot, E.P. Ricci, R. Mourad et al. Loop extrusion as a mechanism for formation of dna damage repair foci, *Nature* **590**, 660 (2021)
- [14] R. Oldenkamp, B.D. Rowland. A walk through the smc cycle: From catching dnas to shaping the genome, *Mol. Cell* **82**, 1616 (2022)
- [15] I.A. Shaltiel, S. Datta, L. Lecomte, M. Hassler, M. Kschonsak, S. Bravo, C. Stober, J. Ormanns, S. Eustermann, C.H. Haering. A hold-and-feed mechanism drives directional dna loop extrusion by condensin, *Science* **376**, 1087 (2022)
- [16] E. Kim, R. Barth, C. Dekker. Looping the genome with smc complexes, *Annu. Rev. Biochem.* **92**, 15 (2023)
- [17] S. Yatskevich, J. Rhodes, K. Nasmyth. Organization of chromosomal dna by smc complexes, *Annu. Rev. Genet.* **53**, 445 (2019)
- [18] T. Hirano. At the heart of the chromosome: SMC proteins in action, *Nat. Rev. Mol. Cell Biol.* **7**, 311 (2006)

[19] M. Hassler, I.A. Shaltiel, M. Kschonsak, B. Simon, F. Merkel, L. Thärichen, H.J. Bailey, J. Macošek, S. Bravo, J. Metz et al. Structural basis of an asymmetric condensin atpase cycle, *Mol. Cell* **74**, 1175 (2019)

[20] R. Takaki, A. Dey, G. Shi, D. Thirumalai. Theory and simulations of condensin mediated loop extrusion in dna, *Nat. Commun.* **12**, 5865 (2021)

[21] B.G. Lee, J. Rhodes, J. Löwe. Clamping of dna shuts the condensin neck gate, *Proc. Natl. Acad. Sci. U. S. A.* **119**, e2120006119 (2022)

[22] M. Kschonsak, F. Merkel, S. Bisht, J. Metz, V. Rybin, M. Hassler, C.H. Haering. Structural basis for a safety-belt mechanism that anchors condensin to chromosomes, *Cell* **171**, 588 (2017)

[23] I. Piazza, A. Rutkowska, A. Ori, M. Walczak, J. Metz, V. Pelechano, M. Beck, C.H. Haering. Association of condensin with chromosomes depends on dna binding by its heat-repeat subunits, *Nat. Struct. Mol. Biol.* **21**, 560 (2014)

[24] J.M. Eeftens, S. Bisht, J. Kerssemakers, M. Kschonsak, C.H. Haering, C. Dekker. Real-time detection of condensin-driven dna compaction reveals a multistep binding mechanism, *EMBO J.* **36**, 3448 (2017)

[25] S. Cuylen, J. Metz, C.H. Haering. Condensin structures chromosomal dna through topological links, *Nat. Struct. Mol. Biol.* **18**, 894 (2011)

[26] Z. Shi, H. Gao, X.c. Bai, H. Yu. Cryo-em structure of the human cohesin-nipbl-dna complex, *Science* **368**, 1454 (2020)

[27] T.L. Higashi, P. Eickhoff, J.S. Sousa, J. Locke, A. Nans, H.R. Flynn, A.P. Snijders, G. Papageorgiou, N. O'reilly, Z.A. Chen et al. A structure-based mechanism for dna entry into the cohesin ring, *Mol* **79**, 917 (2020)

[28] J.E. Collier, B.G. Lee, M.B. Roig, S. Yatskevich, N.J. Petela, J. Metson, M. Voulgaris, A. Gonzalez Llamazares, J. Löwe, K.A. Nasmyth. Transport of dna within cohesin involves clamping on top of engaged heads by scc2 and entrapment within the ring by scc3, *elife* **9**, e59560 (2020)

[29] T.G. Gligoris, J.C. Scheinost, F. Bürmann, N. Petela, K.L. Chan, P. Uluocak, F. Beckouët, S. Gruber, K. Nasmyth, J. Löwe. Closing the cohesin ring: structure and function of its smc3-kleisin interface, *Science* **346**, 963 (2014)

[30] C.H. Haering, A.M. Farcas, P. Arumugam, J. Metson, K. Nasmyth. The cohesin ring concatenates sister dna molecules, *Nature* **454**, 297 (2008)

[31] M. Srinivasan, J.C. Scheinost, N.J. Petela, T.G. Gligoris, M. Wissler, S. Ogushi, J.E. Collier, M. Voulgaris, A. Kurze, K.L. Chan et al. The cohesin ring uses its hinge to organize dna using non-topological as well as topological mechanisms, *Cell* **173**, 1508 (2018)

[32] Y. Kim, Z. Shi, H. Zhang, I.J. Finkelstein, H. Yu. Human cohesin compacts dna by loop extrusion, *Science* **366**, 1345 (2019)

[33] Y. Li, K.W. Muir, M.W. Bowler, J. Metz, C.H. Haering, D. Panne. Structural basis for scc3-dependent cohesin recruitment to chromatin, *elife* **7**, e38356 (2018)

[34] B. Pradhan, T. Kanno, M. Umeda Igarashi, M.S. Loke, M.D. Baaske, J.S.K. Wong, K. Jeppsson, C. Björkegren, E. Kim. The smc5/6 complex is a dna loop-extruding motor, *Nature* **616**, 843 (2023)

[35] A.D. Swett, Z. Tothova. Cohesin mutations and chromatin changes in cancer, *Int. J. Cancer* (2025)

[36] M. Solé-Ferran, A. Losada. Cohesin in 3d: development, differentiation, and disease, *Genes. Dev.* **39**, 679 (2025)

[37] J. Jumper, R. Evans, A. Pritzel, T. Green, M. Figurnov, O. Ronneberger, K. Tunyasuvunakool, R. Bates, A. Žídek, A. Potapenko et al. Highly accurate protein structure prediction with alphafold, *Nature* **596**, 583 (2021)

[38] J. Abramson, J. Adler, J. Dunger, R. Evans, T. Green, A. Pritzel, O. Ronneberger, L. Willmore, A.J. Ballard, J. Bambrick et al. Accurate structure prediction of biomolecular interactions with alphafold 3, *Nature* **630**, 493 (2024)

[39] D. Del Alamo, D. Sala, H.S. Mchaourab, J. Meiler. Sampling alternative conformational states of transporters and receptors with alphafold2, *elife* **11**, e75751 (2022)

[40] X. Guan, Q.Y. Tang, W. Ren, M. Chen, W. Wang, P.G. Wolynes, W. Li. Predicting protein conformational motions using energetic frustration analysis and alphafold2, *Proc. Natl. Acad. Sci. U. S. A.* **121**, e2410662121 (2024)

[41] H.B. Guo, A. Perminov, S. Bekele, G. Kedziora, S. Farajollahi, V. Varaljay, K. Hinkle, V. Molinero,

K. Meister, C. Hung et al. Alphafold2 models indicate that protein sequence determines both structure and dynamics, *Sci. Rep.* **12**, 10696 (2022)

[42] A. Jussupow, V.R. Kaila. Effective molecular dynamics from neural network-based structure prediction models, *J. Chem. Theory Comput.* **19**, 1965 (2023)

[43] J.M. McBride, K. Polev, A. Abdurasulov, V. Reinharz, B.A. Grzybowski, T. Tlusty. Alphafold2 can predict single-mutation effects, *Phys. Rev. Lett.* **131**, 218401 (2023)

[44] J.M. McBride, T. Tlusty. Ai-predicted protein deformation encodes energy landscape perturbation, *Phys. Rev. Lett.* **133**, 098401 (2024)

[45] M.S. Valdés-Tresanco, M.E. Valdés-Tresanco, P.A. Valiente, E. Moreno. gmx_mmpbsa: a new tool to perform end-state free energy calculations with gromacs, *J. Chem. Theory Comput.* **17**, 6281 (2021)

[46] B.R. Miller III, T.D. McGee Jr, J.M. Swails, N. Homeyer, H. Gohlke, A.E. Roitberg. Mmpbsa.py: an efficient program for end-state free energy calculations, *J. Chem. Theory Comput.* **8**, 3314 (2012)

[47] R. Rohs, X. Jin, S.M. West, R. Joshi, B. Honig, R.S. Mann. Origins of specificity in protein-dna recognition, *Annu. Rev. Biochem.* **79**, 233 (2010)

[48] X. Robellet, V. Vanoosthuyse, P. Bernard. The loading of condensin in the context of chromatin, *Curr. Genet.* **63**, 577 (2017)

[49] S.E. Halford, J.F. Marko. How do site-specific dna-binding proteins find their targets?, *Nucleic Acids Res.* **32**, 3040 (2004)

[50] I.F. Davidson, D. Goetz, M.P. Zaczek, M.I. Molodtsov, P.J. Huis in't Veld, F. Weissmann, G. Litos, D.A. Cisneros, M. Ocampo-Hafalla, R. Ladurner et al. Rapid movement and transcriptional re-localization of human cohesin on dna, *EMBO J.* **35**, 2671 (2016)

[51] M. Kanke, E. Tahara, P.J. Huis in't Veld, T. Nishiyama. Cohesin acetylation and wapl-pds5 oppositely regulate translocation of cohesin along dna, *EMBO J.* **35**, 2686 (2016)

[52] H. Kim, J.J. Loparo. Multistep assembly of dna condensation clusters by smc, *Nat. Commun.* **7**, 10200 (2016)

[53] J. Stigler, G.Ö. Çamdere, D.E. Koshland, E.C. Greene. Single-molecule imaging reveals a collapsed conformational state for dna-bound cohesin, *Cell Rep.* **15**, 988 (2016)

[54] E.J. Banigan, A.A. van den Berg, H.B. Brandão, J.F. Marko, L.A. Mirny. Chromosome organization by one-sided and two-sided loop extrusion, *eLife* **9**, e53558 (2020)

[55] R.B. Best, G. Hummer, W.A. Eaton. Native contacts determine protein folding mechanisms in atomistic simulations, *Proc. Natl. Acad. Sci. U. S. A.* **110**, 17874 (2013)

[56] A. Takemoto, K. Kimura, J. Yanagisawa, S. Yokoyama, F. Hanaoka. Negative regulation of condensin i by ck2-mediated phosphorylation, *EMBO J.* **25**, 5339 (2006)

[57] Y. Kagami, K. Nihira, S. Wada, M. Ono, M. Honda, K. Yoshida. Mps1 phosphorylation of condensin ii controls chromosome condensation at the onset of mitosis, *J. Cell Biol.* **205**, 781 (2014)

[58] S. Tane, K. Shintomi, K. Kinoshita, Y. Tsubota, M.M. Yoshida, T. Nishiyama, T. Hirano. Cell cycle-specific loading of condensin i is regulated by the n-terminal tail of its kleisin subunit, *Elife* **11**, e84694 (2022)

[59] Z.F. Brotzakis, S. Zhang, M.H. Murtada, M. Vendruscolo. Alphafold prediction of structural ensembles of disordered proteins, *Nat. Commun.* **16**, 1632 (2025)

[60] H. Koide, N. Kodera, S. Bisht, S. Takada, T. Terakawa. Modeling of dna binding to the condensin hinge domain using molecular dynamics simulations guided by atomic force microscopy, *PLoS Comput. Biol.* **17**, e1009265 (2021)

[61] F. Nagae, Y. Murayama, T. Terakawa. Molecular mechanism of parental h3/h4 recycling at a replication fork, *Nat. Commun.* **15**, 9485 (2024)

[62] F. Nagae, S. Takada, T. Terakawa. Histone chaperone nap1 dismantles an h2a/h2b dimer from a partially unwrapped nucleosome, *Nucleic Acids Res.* **51**, 5351 (2023)

[63] K. Inoue, S. Takada, T. Terakawa. Coarse-grained molecular dynamics simulations of base-pair mismatch recognition protein muts sliding along dna, *Biophys. Physicobiol.* **19**, e190015 (2022)

[64] F. Nagae, G.B. Brandani, S. Takada, T. Terakawa. The lane-switch mechanism for nucleosome repositioning by dna translocase, *Nucleic Acids Res.* **49**, 9066 (2021)

[65] S. Takada, R. Kanada, C. Tan, T. Terakawa, W. Li, H. Kenzaki. Modeling structural dynamics of biomolecular complexes by coarse-grained molecular simulations, *Acc. Chem. Res.* **48**, 3026 (2015)

[66] S. Kmiecik, D. Gront, M. Kolinski, L. Wieteska, A.E. Dawid, A. Kolinski. Coarse-grained protein models and their applications, *Chem. Rev.* **116**, 7898 (2016)

[67] W.G. Noid. Perspective: Coarse-grained models for biomolecular systems, *J. of Chem. Phys.* **139** (2013)

[68] J.W. Tworek, A.H. Elcock. Orientationally averaged version of the rotne–prager–yamakawa tensor provides a fast but still accurate treatment of hydrodynamic interactions in brownian dynamics simulations of biological macromolecules, *J. Chem. Theory Comput.* **19**, 5099 (2023)

[69] J. Roel-Touris, A.M. Bonvin. Coarse-grained (hybrid) integrative modeling of biomolecular interactions, *Comput. Struct. Biotechnol. J.* **18**, 1182 (2020)

[70] Y. Wang, X. Chu, S. Longhi, P. Roche, W. Han, E. Wang, J. Wang. Multiscaled exploration of coupled folding and binding of an intrinsically disordered molecular recognition element in measles virus nucleoprotein, *Proc. Natl. Acad. Sci. U. S. A.* **110**, E3743 (2013)

[71] H. Koide, N. Kodera, S. Takada, T. Terakawa. Solution afm imaging and coarse-grained molecular modeling of yeast condensin structural variation coupled to the atp hydrolysis cycle, *J. Mol. Biol.* p. 169185 (2025)

[72] K. Kimura, T. Hirano. Atp-dependent positive supercoiling of dna by 13s condensin: a biochemical implication for chromosome condensation, *Cell* **90**, 625 (1997)

[73] M. Kong, E.E. Cutts, D. Pan, F. Beuron, T. Kaliyappan, C. Xue, E.P. Morris, A. Musacchio, A. Vannini, E.C. Greene. Human condensin i and ii drive extensive atp-dependent compaction of nucleosome-bound dna, *Mol. Cell* **79**, 99 (2020)

[74] A. Borsellini, D. Conti, E.E. Cutts, R.J. Harris, K. Walstein, A. Graziadei, V. Cecatiello, T.F. Aarts, R. Xie, A. Mazouzi et al. Condensin ii activation by m18bp1, *Mol. Cell* **85**, 2688 (2025)

[75] Y. Yu, S. Li, Z. Ser, H. Kuang, T. Than, D. Guan, X. Zhao, D.J. Patel. Cryo-em structure of dna-bound smc5/6 reveals dna clamping enabled by multi-subunit conformational changes, *Proc. Natl. Acad. Sci. U. S. A.* **119**, e2202799119 (2022)

[76] V. Vennelakanti, A. Nazemi, R. Mehmood, A.H. Steeves, H.J. Kulik. Harder, better, faster, stronger: Large-scale qm and qm/mm for predictive modeling in enzymes and proteins, *Curr. Opin. Struct. Biol.* **72**, 9 (2022)

[77] T. Kubář, M. Elstner, Q. Cui. Hybrid quantum mechanical/molecular mechanical methods for studying energy transduction in biomolecular machines, *Annu. Rev. Biophys.* **52**, 525 (2023)

[78] T.L. Higashi, F. Uhlmann. Smc complexes: Lifting the lid on loop extrusion, *Curr. Opin. Cell Biol.* **74**, 13 (2022)

[79] B. Webb, A. Sali. Comparative protein structure modeling using modeller, *Curr. Protoc. Bioinf.* **54**, 5 (2016)

[80] S. Jo, J.B. Lim, J.B. Klauda, W. Im. Charmm-gui membrane builder for mixed bilayers and its application to yeast membranes, *Biophys. J.* **97**, 50 (2009)

[81] J. Huang, S. Rauscher, G. Nawrocki, T. Ran, M. Feig, B.L. De Groot, H. Grubmüller, A.D. MacKerell Jr. Charmm36m: an improved force field for folded and intrinsically disordered proteins, *Nat. Methods* **14**, 71 (2017)

[82] M.J. Abraham, T. Murtola, R. Schulz, S. Páll, J.C. Smith, B. Hess, E. Lindahl. Gromacs: High performance molecular simulations through multi-level parallelism from laptops to supercomputers, *SoftwareX* **1**, 19 (2015)

[83] W. Li, W. Wang, S. Takada. Energy landscape views for interplays among folding, binding, and allostery of calmodulin domains, *Proc. Natl. Acad. Sci. U. S. A.* **111**, 10550 (2014)

[84] W. Li, T. Terakawa, W. Wang, S. Takada. Energy landscape and multiroute folding of topologically complex proteins adenylate kinase and 2ouf-knot, *Proc. Natl. Acad. Sci. U. S. A.* **109**, 17789 (2012)

[85] W. Li, H. Yoshii, N. Hori, T. Kameda, S. Takada. Multiscale methods for protein folding simulations, *Methods* **52**, 106 (2010)

[86] T. Terakawa, S. Takada. Multiscale ensemble modeling of intrinsically disordered proteins: p53 n-terminal domain, *Biophys. J.* **101**, 1450 (2011)

[87] G.S. Freeman, D.M. Hinckley, J.P. Lequieu, J.K. Whitmer, J.J. De Pablo. Coarse-grained modeling of dna curvature, *J. Chem. Phys.* **141** (2014)

[88] T. Niina, G.B. Brandani, C. Tan, S. Takada. Sequence-dependent nucleosome sliding in rotation-coupled and uncoupled modes revealed by molecular simulations, *PLoS Comput. Biol.* **13**, e1005880 (2017)

[89] T. Veitshans, D. Klimov, D. Thirumalai. Protein folding kinetics: timescales, pathways and energy landscapes in terms of sequence-dependent properties, *Folding Des.* **2**, 1 (1997)

[90] D.M. Hinckley, G.S. Freeman, J.K. Whitmer, J.J. De Pablo. An experimentally-informed coarse-grained 3-site-per-nucleotide model of dna: Structure, thermodynamics, and dynamics of hybridization, *J. Chem. Phys.* **139** (2013)

[91] C. Tan, T. Terakawa, S. Takada. Dynamic coupling among protein binding, sliding, and dna bending revealed by molecular dynamics, *J. Am. Chem. Soc.* **138**, 8512 (2016)

[92] G.S. Freeman, J.P. Lequieu, D.M. Hinckley, J.K. Whitmer, J.J. De Pablo. Dna shape dominates sequence affinity in nucleosome formation, *Phys. Rev. Lett.* **113**, 168101 (2014)

[93] J. Jung, K. Yagi, C. Tan, H. Oshima, T. Mori, I. Yu, Y. Matsunaga, C. Kobayashi, S. Ito, D. Ugarte La Torre et al. Genesis 2.1: High-performance molecular dynamics software for enhanced sampling and free-energy calculations for atomistic, coarse-grained, and quantum mechanics/molecular mechanics models, *J. Phys. Chem. B* **128**, 6028 (2024)

[94] W. Humphrey, A. Dalke, K. Schulten. Vmd: visual molecular dynamics, *J. Mol. Graph.* **14**, 33 (1996)

[95] L. Schrodinger. The pymol molecular graphics system, *Version 1*, 8 (2015)

[96] G.A. Tribello, M. Bonomi, D. Branduardi, C. Camilloni, G. Bussi. Plumed 2: New feathers for an old bird, *Comput. Phys. Commun.* **185**, 604 (2014)

[97] G. Bussi, G.A. Tribello. Analyzing and biasing simulations with plumed, *Methods Mol. Biol.* **2022**, 529 (2019)

[98] Y. Wang, R.H. Austin, E.C. Cox. Single molecule measurements of repressor protein 1d diffusion on dna, *Phys. Rev. Lett.* **97**, 048302 (2006)

[99] X. Chu, V. Muñoz. Roles of conformational disorder and downhill folding in modulating protein–dna recognition, *Phys. Chem. Chem. Phys.* **19**, 28527 (2017)

[100] N. Michaud-Agrawal, E.J. Denning, T.B. Woolf, O. Beckstein. Mdanalysis: a toolkit for the analysis of molecular dynamics simulations, *J. Comput. Chem.* **32**, 2319 (2011)

[101] E.H. Spanier, E.H. Spanier, *Algebraic topology* (Springer Science & Business Media, 1989)

Acknowledgements

X.C. thanks Prof. Qianyuan Tang for the useful discussion. X.C. acknowledges support from the National Natural Science Foundation of China (Grant Nos. 32201020 and 12474201), the General Program of the Guangdong Basic and Applied Basic Research Foundation (Grant No. 2024A1515010862), the Guangdong Provincial Project (Grant No. 2023QN10X037) and the Guangdong S&T Program (Grant No. 2025A0505000027). Y.W. thanks the Information Technology Center and State Key Lab of CAD&CG, Zhejiang University, for computational support. The authors also acknowledge the Green e Materials Laboratory (GeM) and HPC+AI Intelligence Computing Center at the Hong Kong University of Science and Technology (Guangzhou) for providing computational support.

Author contributions

J.C. and X.C. conceived the overall study. J.C. performed and analyzed all simulations under the supervision of X.C. X.C., Y.W. and C.F. participated in discussions during the study and contributed to the development of the methodology. J.C. wrote the first draft of the manuscript with input from X.C., Y.W. All authors contributed to the writing of the manuscript.

Competing interests

The authors declare no competing interests.

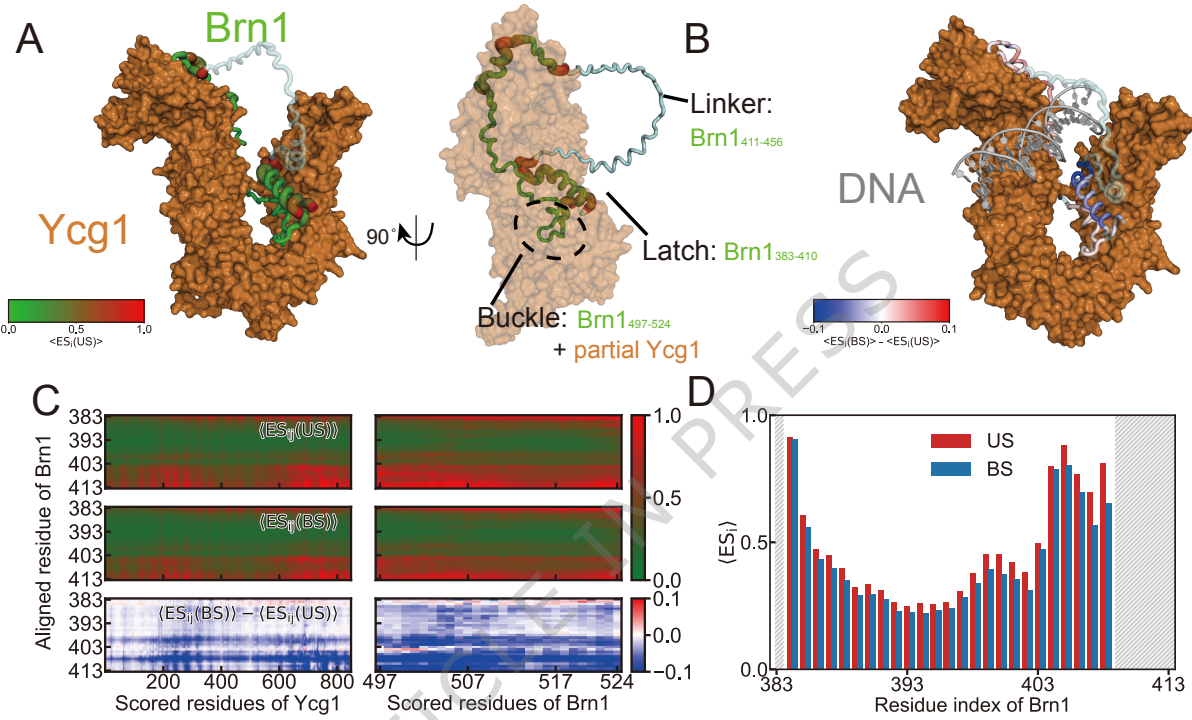


Figure 1: Effective strain in AlphaFold3-predicted Ycg1-Brn1 structures in the DNA-unbound state (US) and DNA-bound state (BS). (A) Residue-wise effective strain $\langle ES_i \rangle$ mapped onto the Brn1 kleisin (residues 383-524) in the US. Tube thickness and a color bar (green→red) indicate increasing $\langle ES_i \rangle$. Pale-cyan, semi-transparent segments mark positions where $\langle ES_i \rangle$ is undefined (see Methods for details). (B) Differences in residue-wise effective strain between the BS and US, $\langle ES_i(BS) \rangle - \langle ES_i(US) \rangle$, projected onto Brn1 in the BS. A blue→white→red scale indicates relative stabilization (values < 0) or destabilization (values > 0) upon DNA binding. (C) Pairwise effective-strain matrices $\langle ES_{ij} \rangle$ and their BS - US differences. Columns correspond to Brn1 latch residues (aligned set); rows include Ycg1 and Brn1 buckle residues (scored set). (D) Per-residue comparison of $\langle ES_i \rangle$ for the BS versus the US across the Brn1 latch residues 383-410. Gray shaded regions indicate residues lacking valid values in one or both states. $\langle ES_i \rangle$ and $\langle ES_{ij} \rangle$ summarize normalized AlphaFold confidence (PAE-based) around residue i and between residue pairs (i, j) , respectively. Lower (higher) values indicate more (less) rigid/consistent relative placement. Formal definitions, normalization, and the residue index map for Ycg1-Brn1 are provided in the Methods and Table S1.

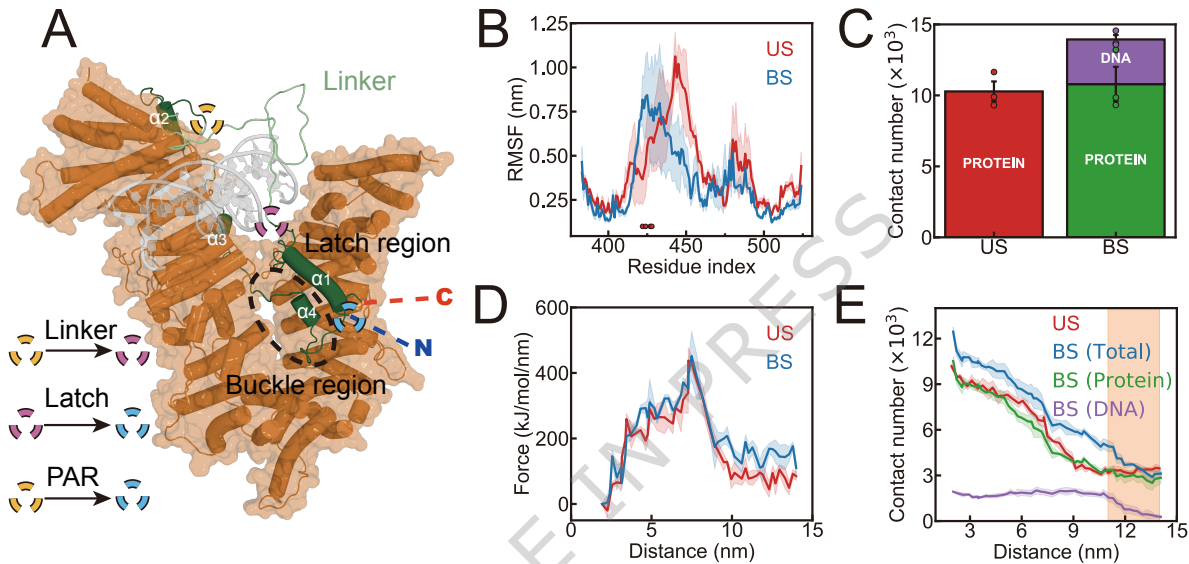


Figure 2: Stabilizing effect of DNA binding on the safety-belt dynamics based on all-atom MD simulations. (A) Structural schematic highlighting functional regions of the condensin protein complex. The Ycg1 HEAT-repeat subunit is shown as an orange surface representation, and Brn1 kleisin is depicted in dark green. The linker region, absent from crystal structures and reconstructed, is shown in pale green. Specific Brn1 helices ($\alpha 1$ - $\alpha 4$) are explicitly labeled for clarity. The C- and N-termini are indicated with red and blue dashed lines, respectively. Functional regions including the latch and buckle are distinctly highlighted, with symbolic representations for linker, latch, and PAR elements provided in the legend. (B) Residue-level RMSF comparison between the US and BS. Negatively charged residues exhibiting higher RMSF in the BS compared to the US are indicated with red circles. (C) Time-dependent contact numbers between the PAR and the rest of the protein complex in the US and BS during unbiased MD simulations. (D) Force profiles versus distance, derived from steered MD simulations. (E) Distance-dependent contact numbers from steered MD simulations. For the BS, contact numbers between PAR and DNA (purple), PAR and the remaining protein (green), and PAR and total remaining components (blue) are shown. For the US, the total contact number between the PAR and remaining components is shown in red. In (B-E), the shadow regions and error bars represent the mean \pm standard error of the mean (SEM) over $n=3$ independent MD simulations.

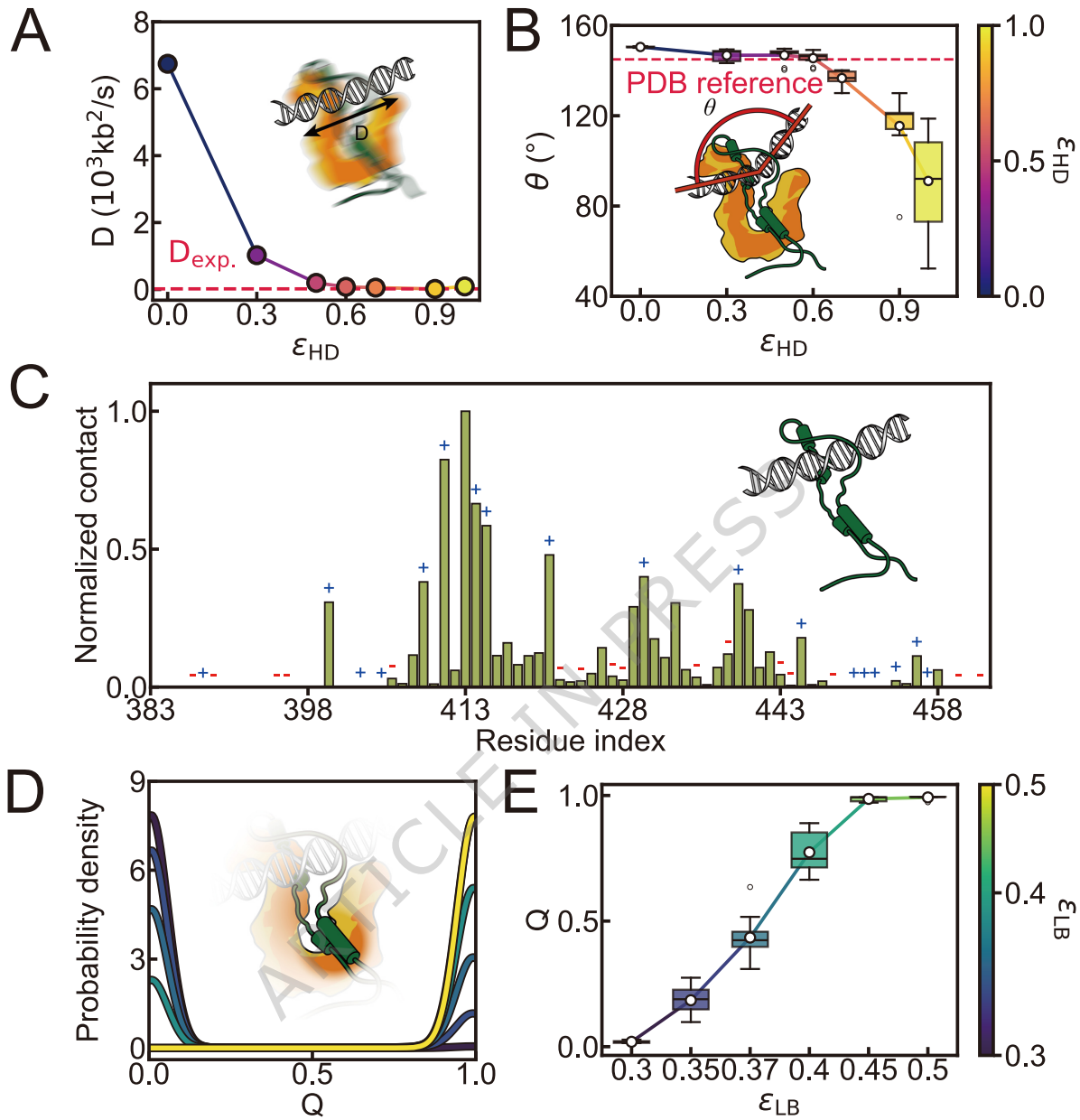


Figure 3: Effect of CG interaction parameters on safety-belt dynamics and DNA properties. (A) Diffusion coefficient D for safety-belt diffusing along naked DNA as a function of the HEAT-DNA interaction strength ε_{HD} . The red dashed line marks an experimentally accessible mean diffusion coefficient reported for cohesin/condensin sliding [54]. Each data point was determined from a linear fit to the mean MSD curve. (B) Mean DNA bending angle versus ε_{HD} . The red dashed line indicates the reference bending angle from the cryo-EM structure (PDB: 7Q2Z) [21]. Box plots indicate the mean (white circle), median (black line), 25th and 75th percentile (box), and the range of data within $1.5 \times$ interquartile range (whiskers), as well as outliers (single points) over $n=10$ independent MD simulations. (C) Normalized contact frequency between DNA and PAR residues 383-456, highlighting residue-level variation. Positively charged residues are marked with blue "+", negatively charged with red "-". (D) Probability density of the latch-buckle order parameter Q for different latch-buckle interaction strengths ε_{LB} (0.30-0.50). Q measures the fraction of latch-buckle native contacts present in the crystal structure. (E) Mean Q as a function of ε_{LB} , showing increased closure/stability with stronger latch-buckle interactions. Box plots indicate the mean (white circle), median (black line), 25th and 75th percentile (box), and the range of data within $1.5 \times$ interquartile range (whiskers), as well as outliers (single points) over $n=10$ independent MD simulations.

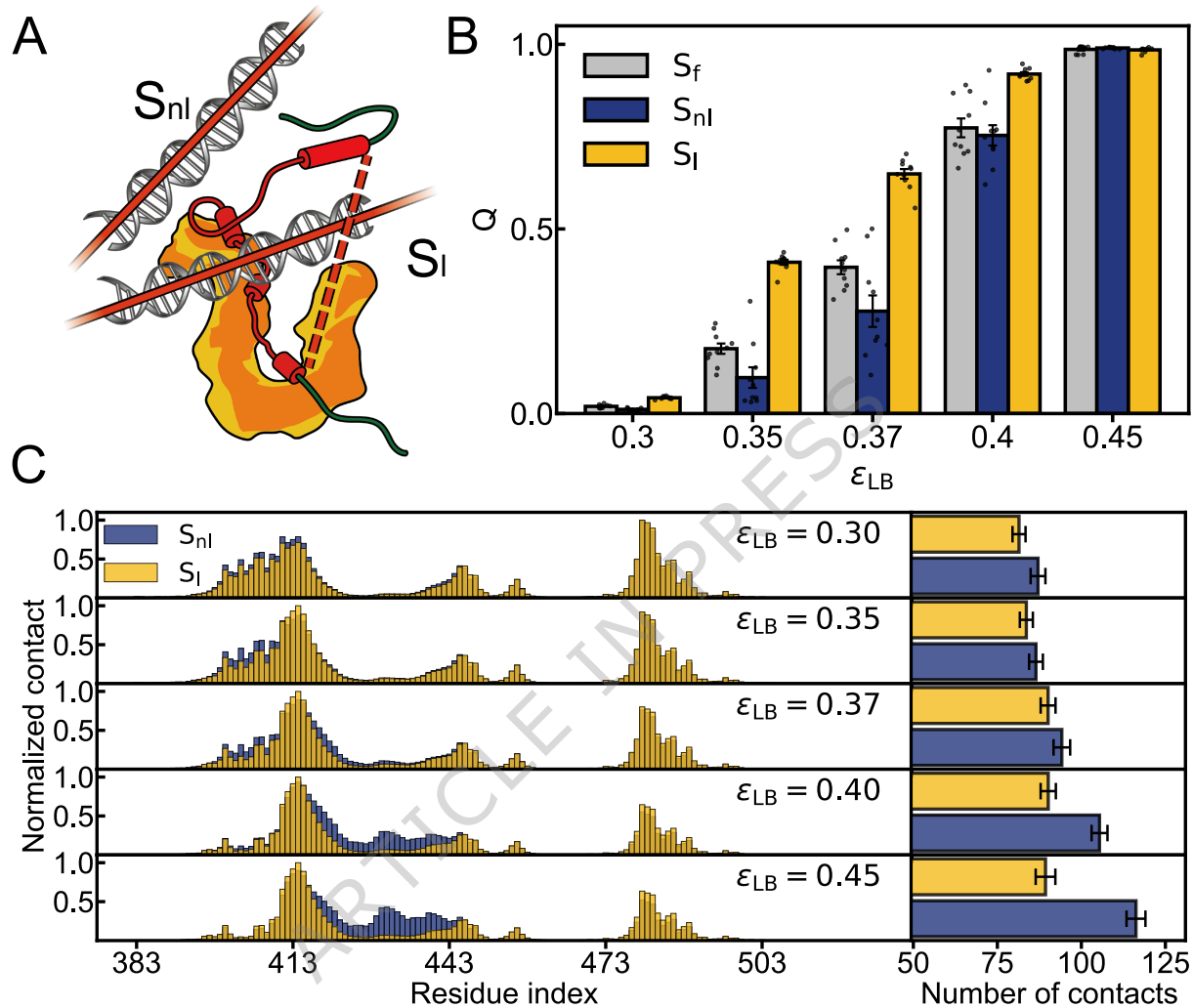


Figure 4: Interactions in condensin safety-belt at the distinct states when DNA is outside and inside the safety-belt loop based on CG MD simulations. (A) Schematic representations of states S_{nl} (“non-looped”) and S_l (“looped”). DNA is modeled as an infinitely large closed loop (red), while the Brn1 loop combined with the dashed segment forms the second closed loop used for calculating the linking number. (B) Fraction of native latch-buckle contacts, Q , in the S_f (DNA-free state), S_{nl} , and S_l as a function of the latch-buckle interaction strength ε_{LB} . The error bars represent the mean \pm SEM ($n = 10$ blocks). For each condition, all qualifying data points from the simulation replicas were pooled together. This collection was then divided into 10 non-overlapping blocks of approximately equal size. The mean of each block is plotted as an individual black dot. (C) DNA-Brn1 contact frequency maps in the S_{nl} and S_l at $\varepsilon_{LB} = 0.30, 0.35, 0.37, 0.40, 0.45$. Contact counts are normalized to the maximum within each panel to highlight residue-level differences; bar plots at right summarize the average contact number per state at each ε_{LB} . Error bars represent the mean \pm SEM over $n=50$ independent MD simulations.

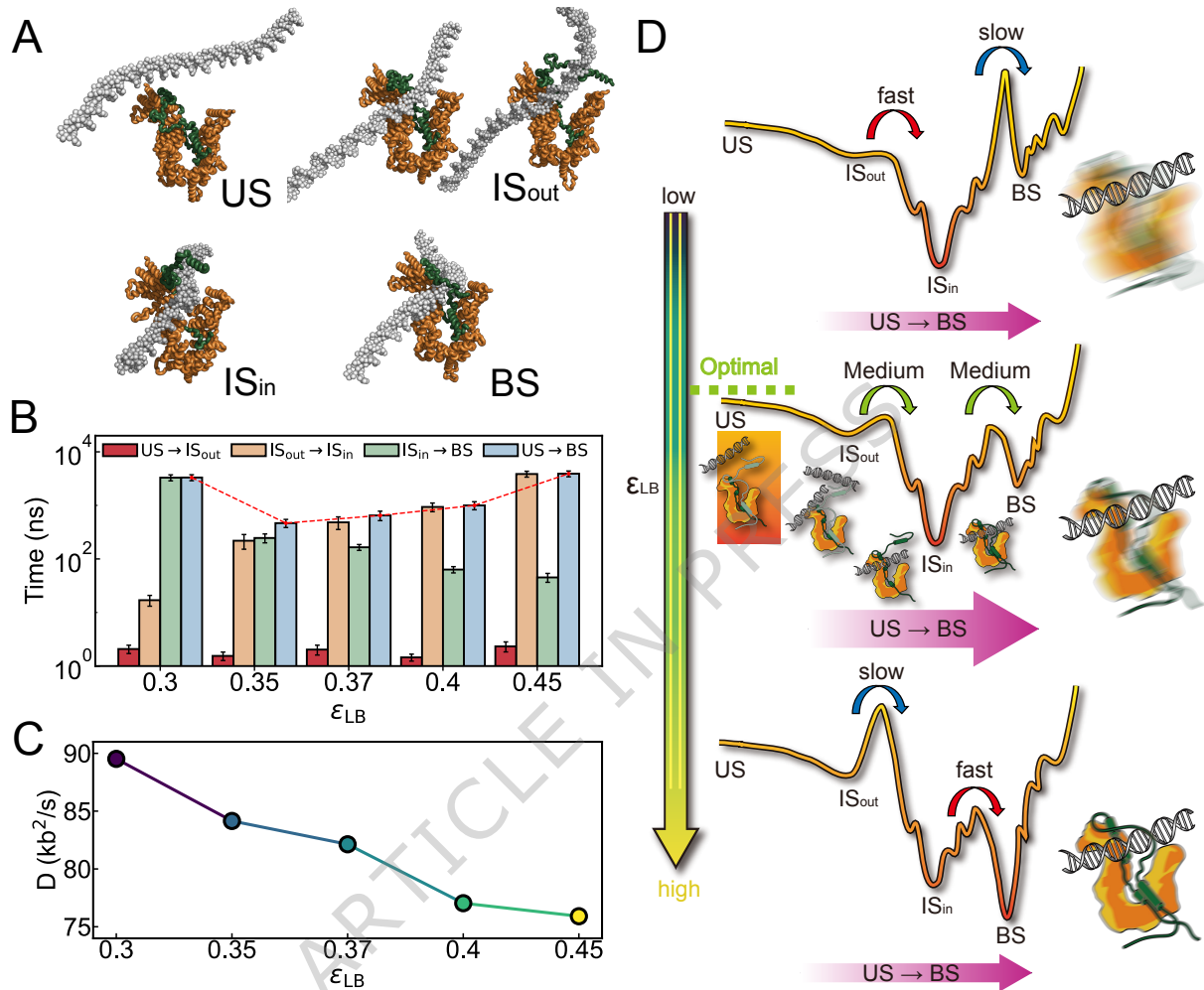


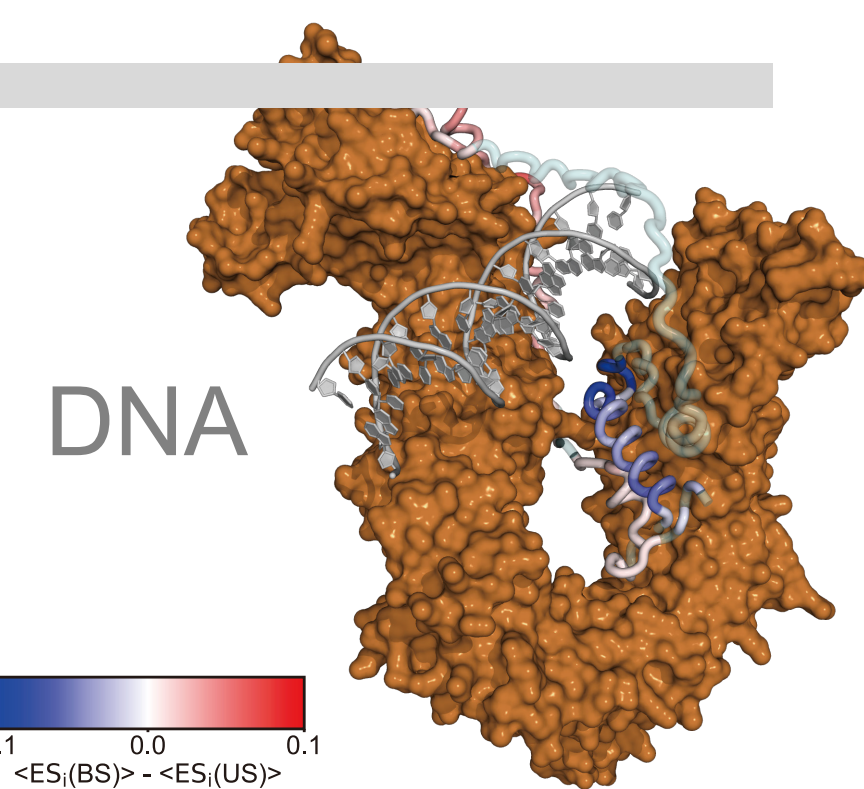
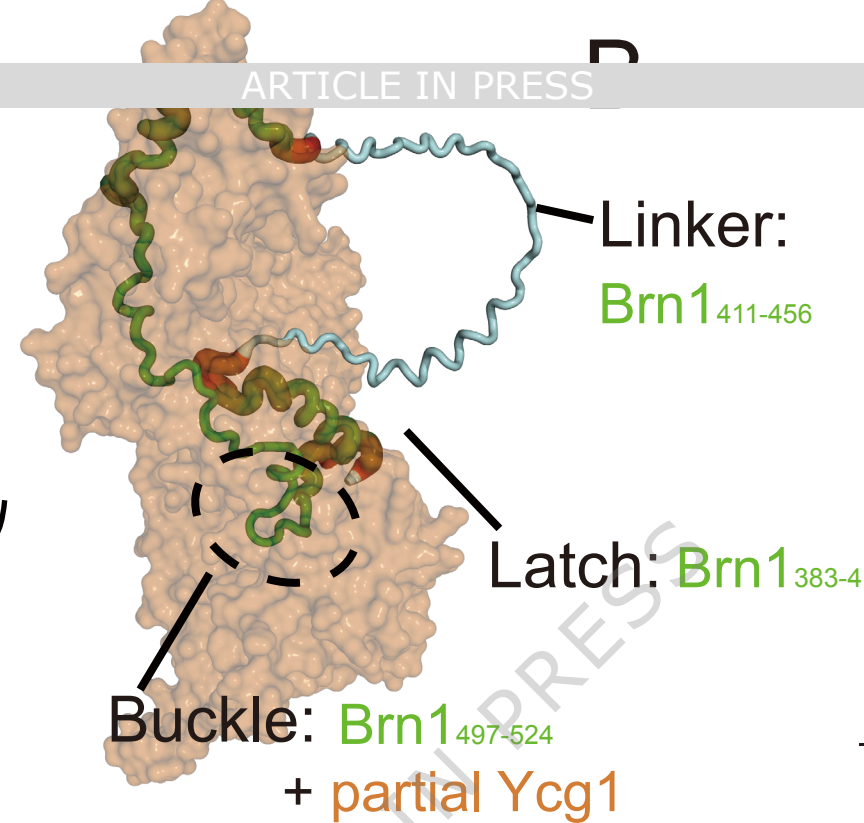
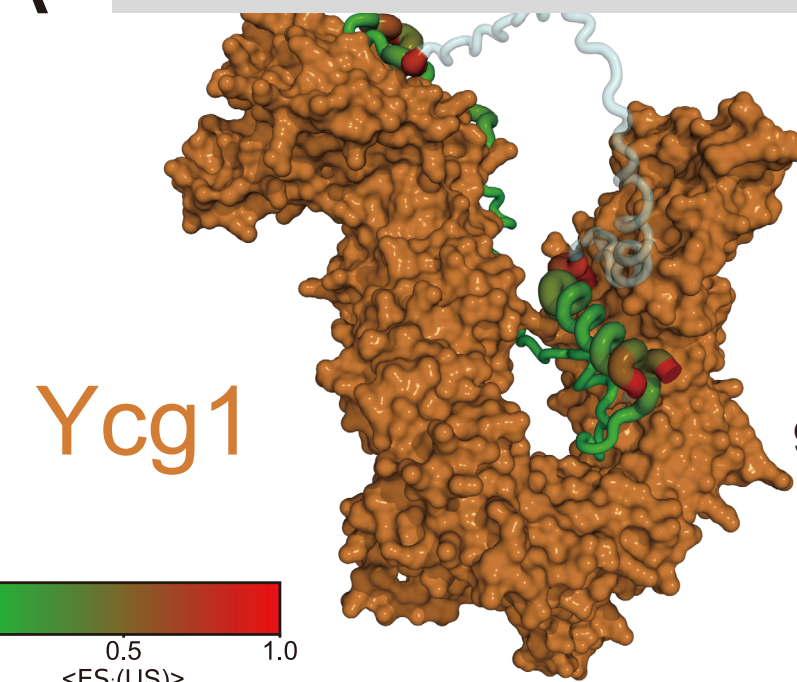
Figure 5: Kinetics of DNA entry via the Ycg1-Brn1 “safety belt” from CG MD simulations. (A) Schematic of four states: unbound (US), intermediate with DNA outside the Brn1 loop (IS_{out}), intermediate with DNA inside the loop (IS_{in}), and bound (BS). IS_{out} is defined solely by the DNA path (outside the loop) and can occur with either an open- or closed-latch, so both configurations are shown. (B) Transition times between these states obtained from simulations tracking DNA movement into the binding pocket formed by the Brn1 loop and Ycg1 (i.e., the “safety belt”). The horizontal axis shows different latch-buckle interaction strengths (ϵ_{LB}), and the vertical axis presents transition times for US \rightarrow IS_{out}, IS_{out} \rightarrow IS_{in}, IS_{in} \rightarrow BS, and US \rightarrow BS. Error bars represent the mean \pm SEM over $n=50$ independent MD simulations. (C) Diffusion coefficients of the safety belt sliding along naked DNA plotted against various ϵ_{LB} values (0.3, 0.35, 0.37, 0.4, 0.45), indicating how latch-buckle interaction strength affects mobility. Each data point was determined from a linear fit to the mean MSD curve. (D) Qualitative free-energy landscapes summarizing dominant pathways and barrier trends en route to the BS (typically US \rightarrow IS_{out} \rightarrow IS_{in} \rightarrow BS) as a function of ϵ_{LB} . Right-side insets schematize the observed change in D with ϵ_{LB} .

A

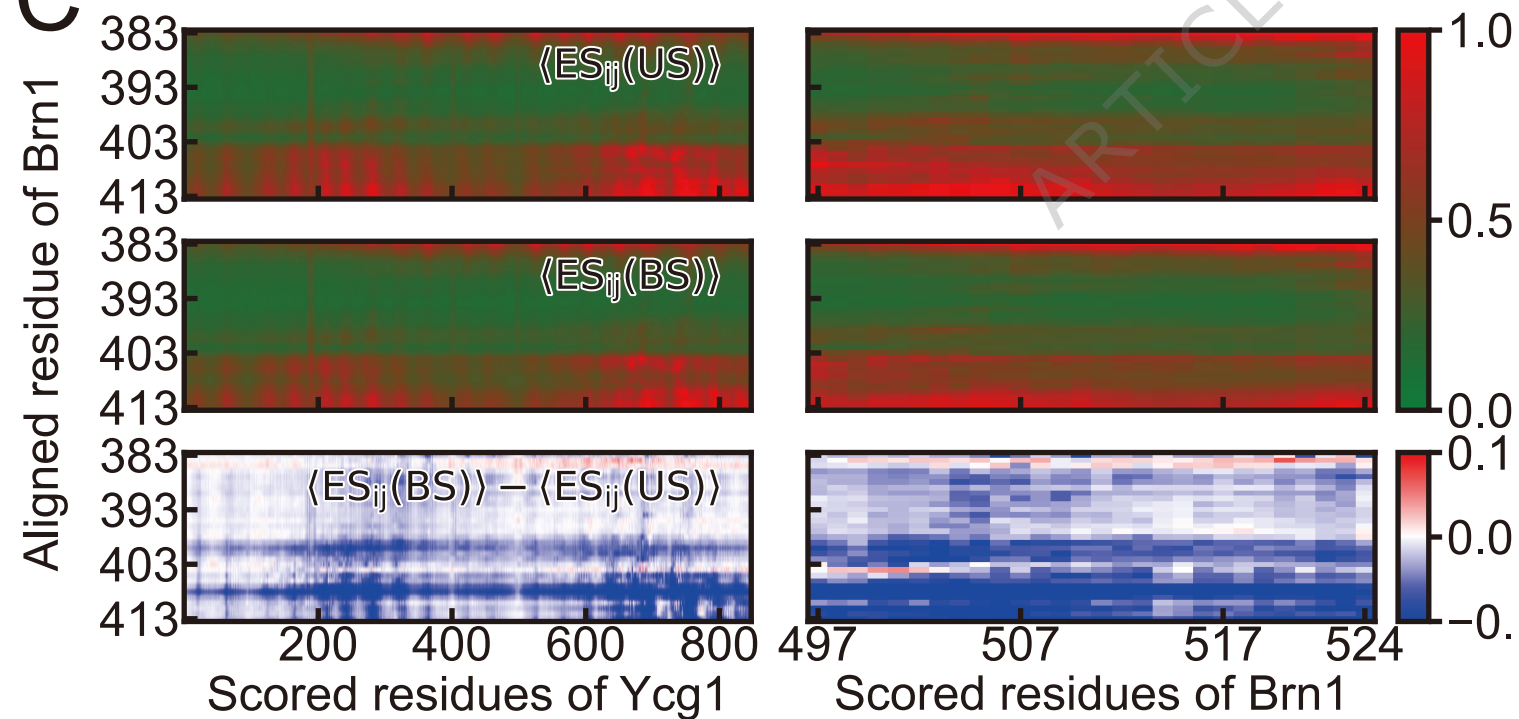
Brn1

ARTICLE IN PRESS

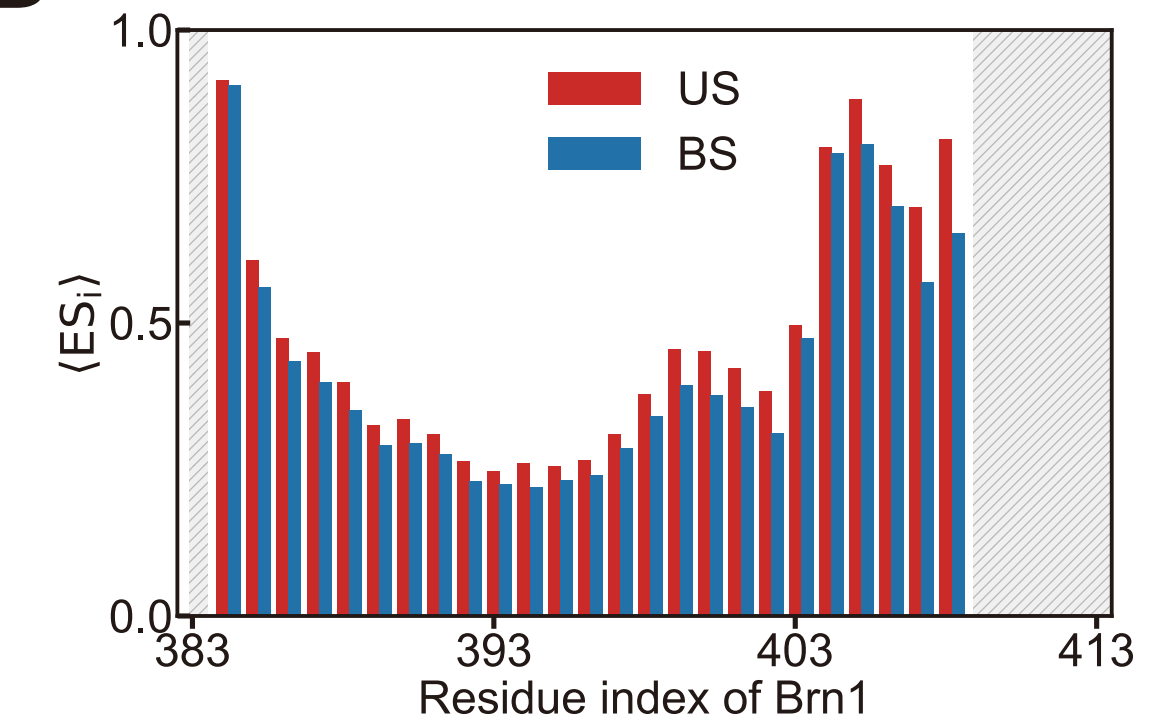
B

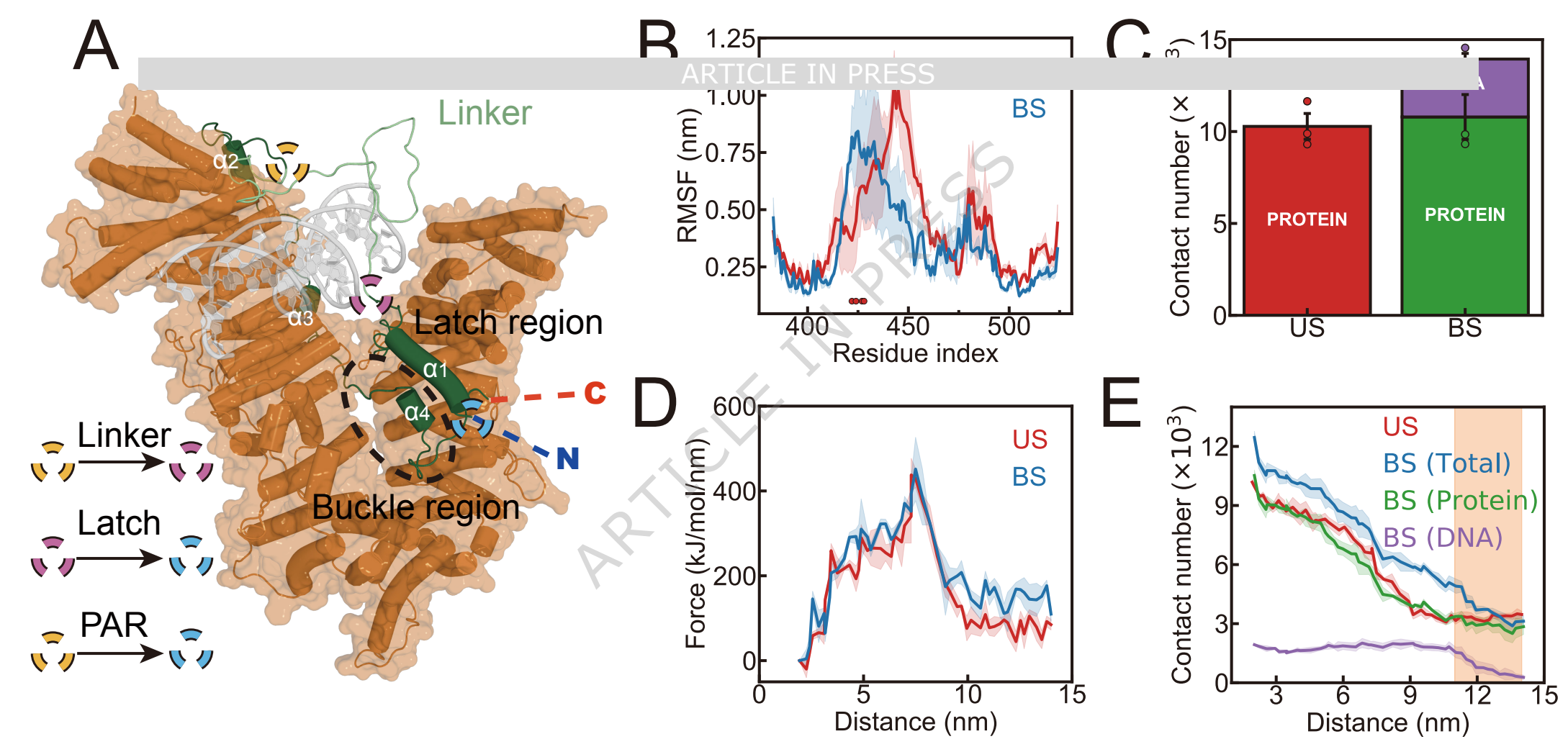


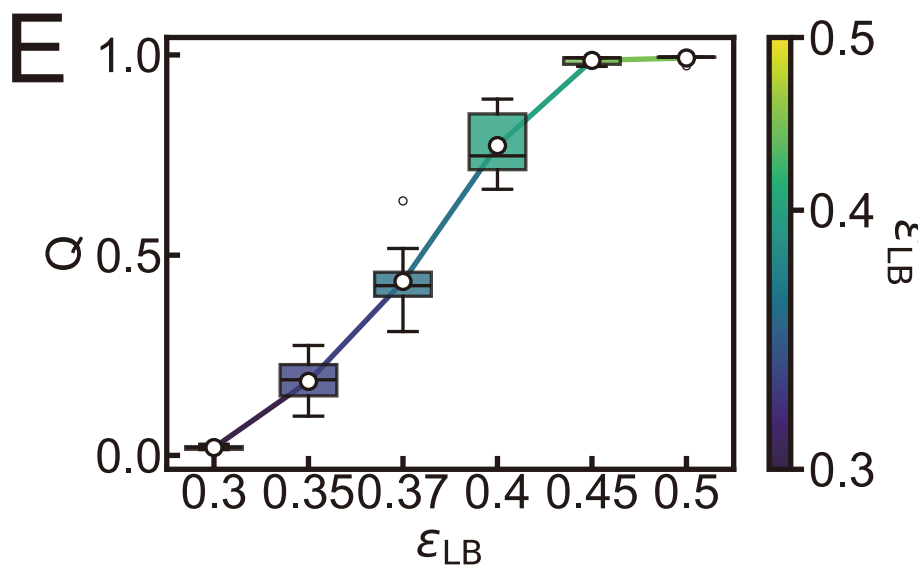
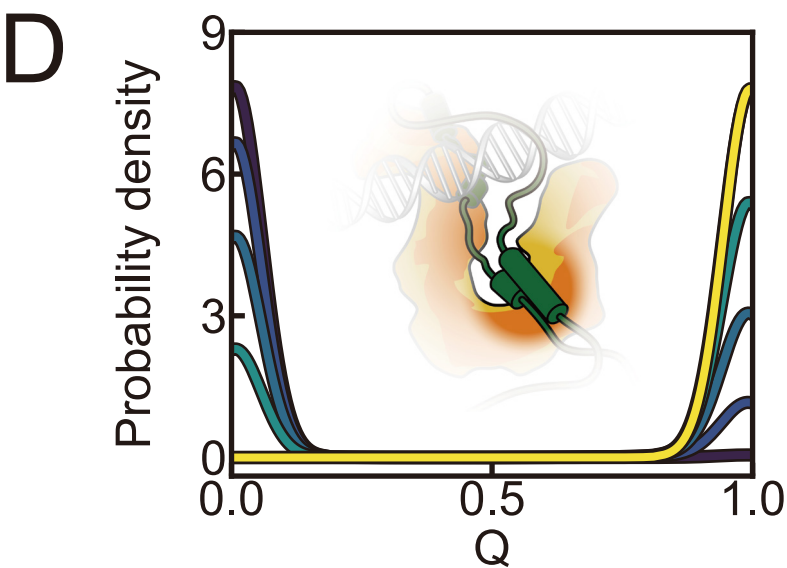
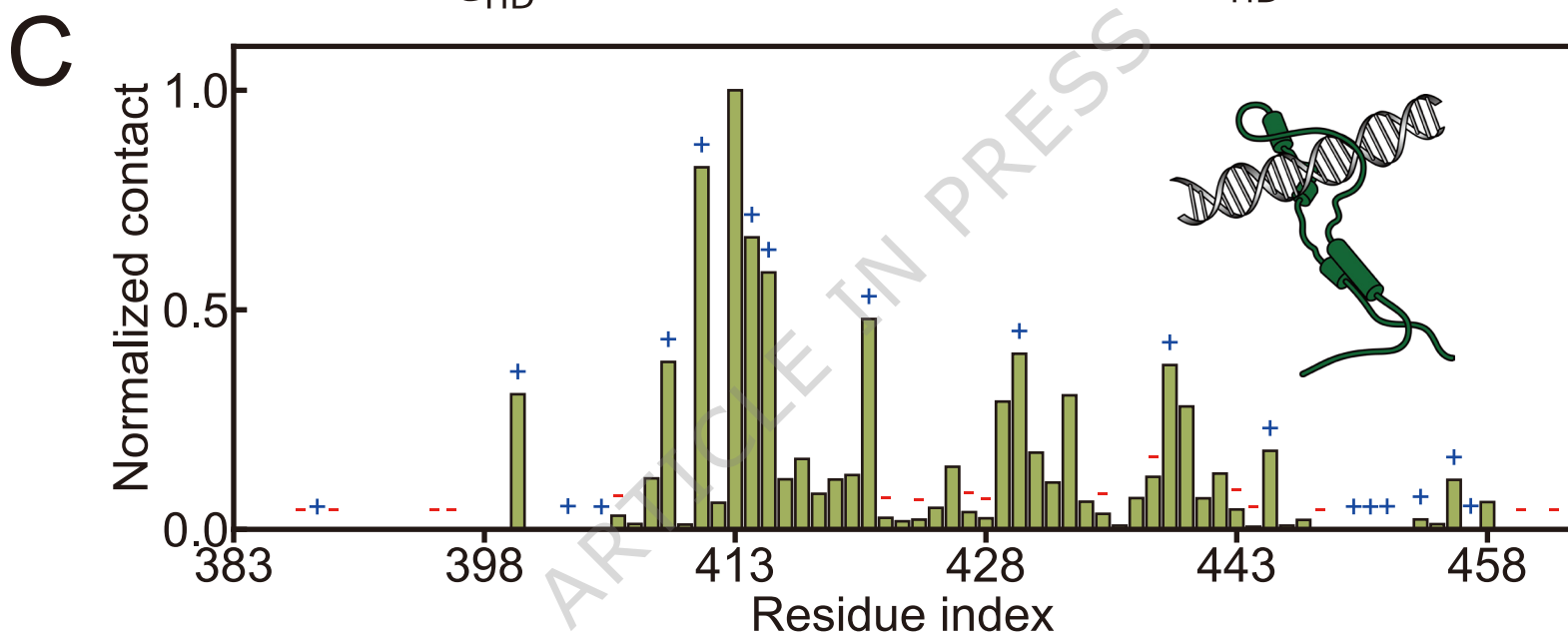
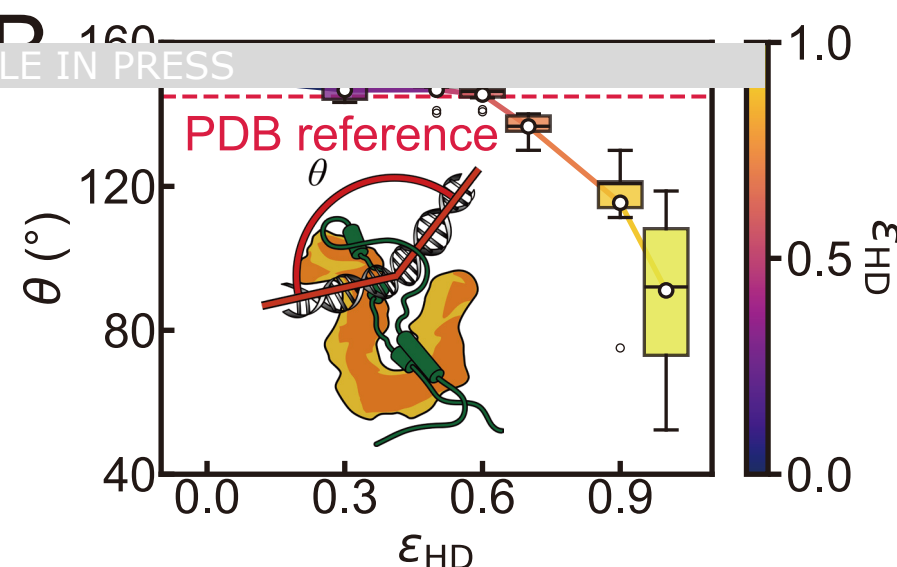
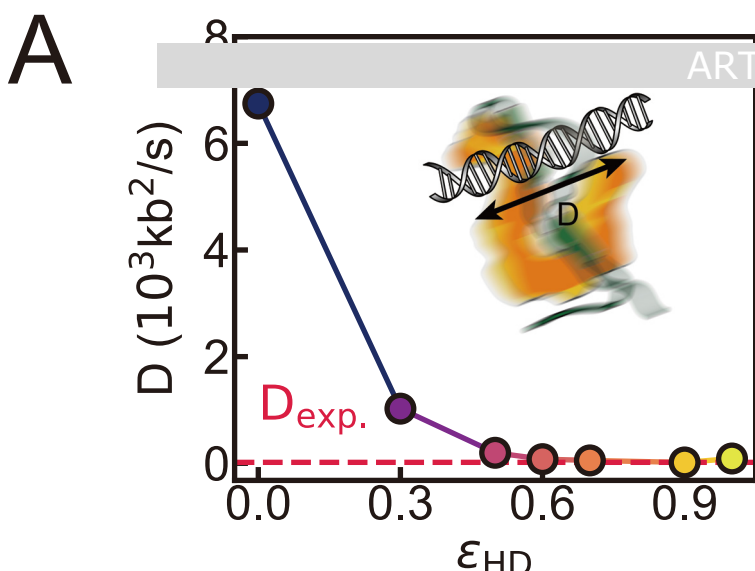
C



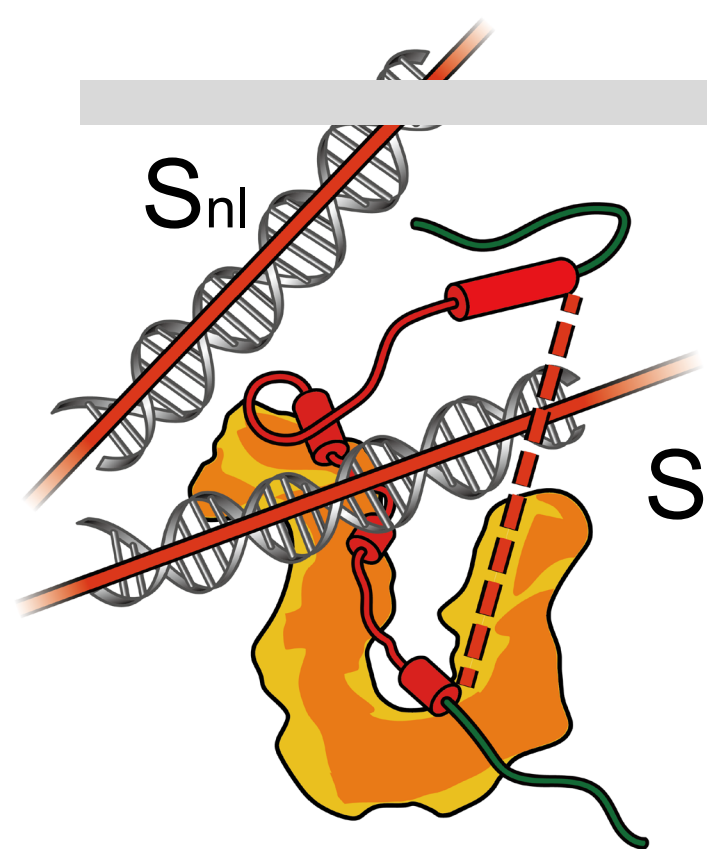
D



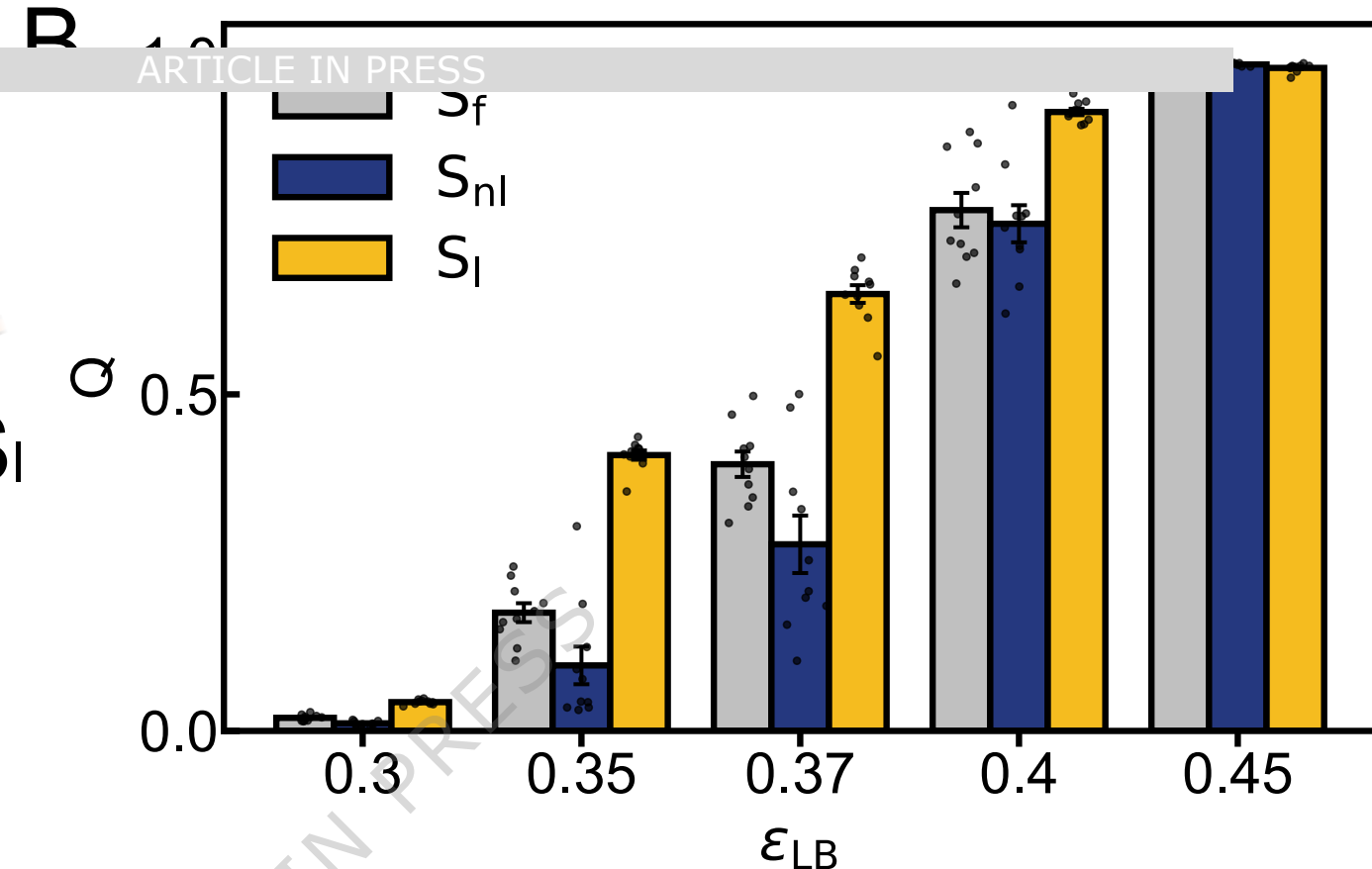




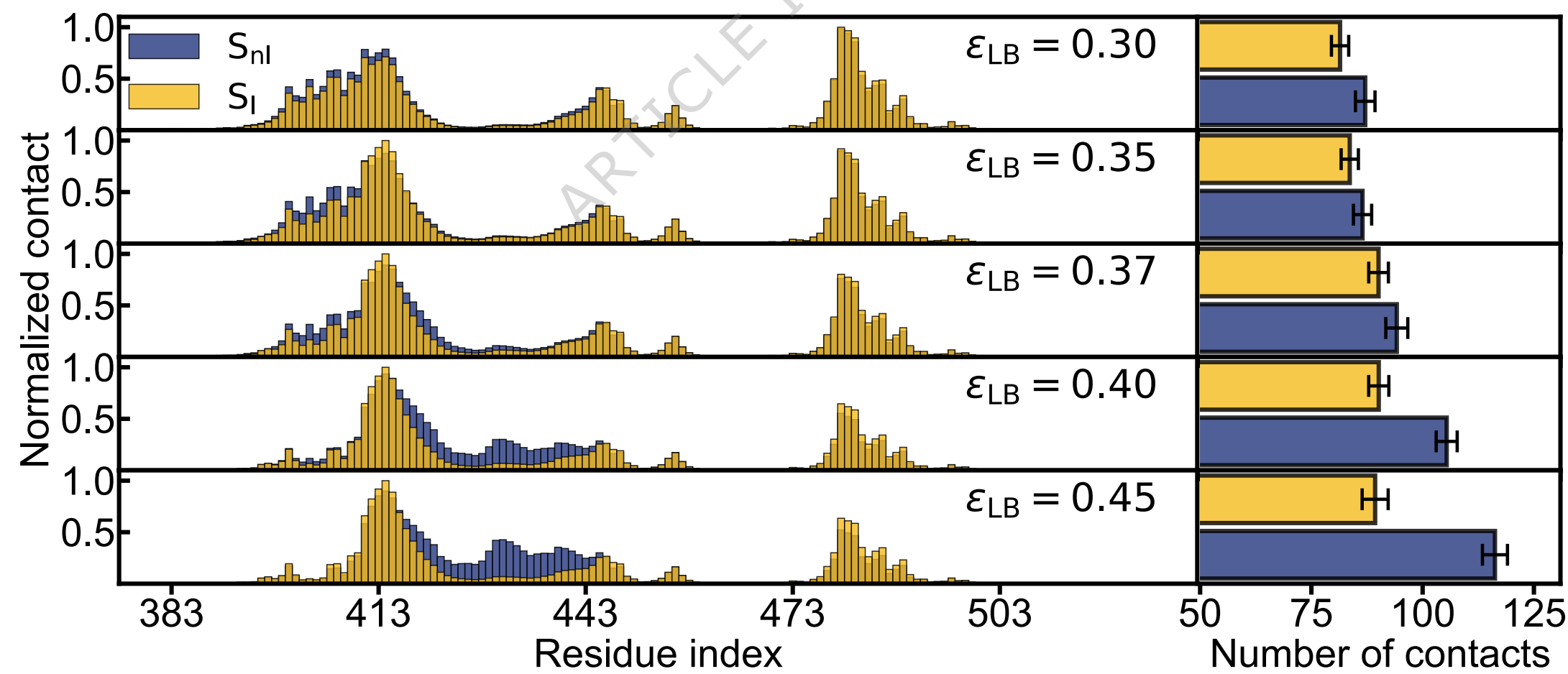
A



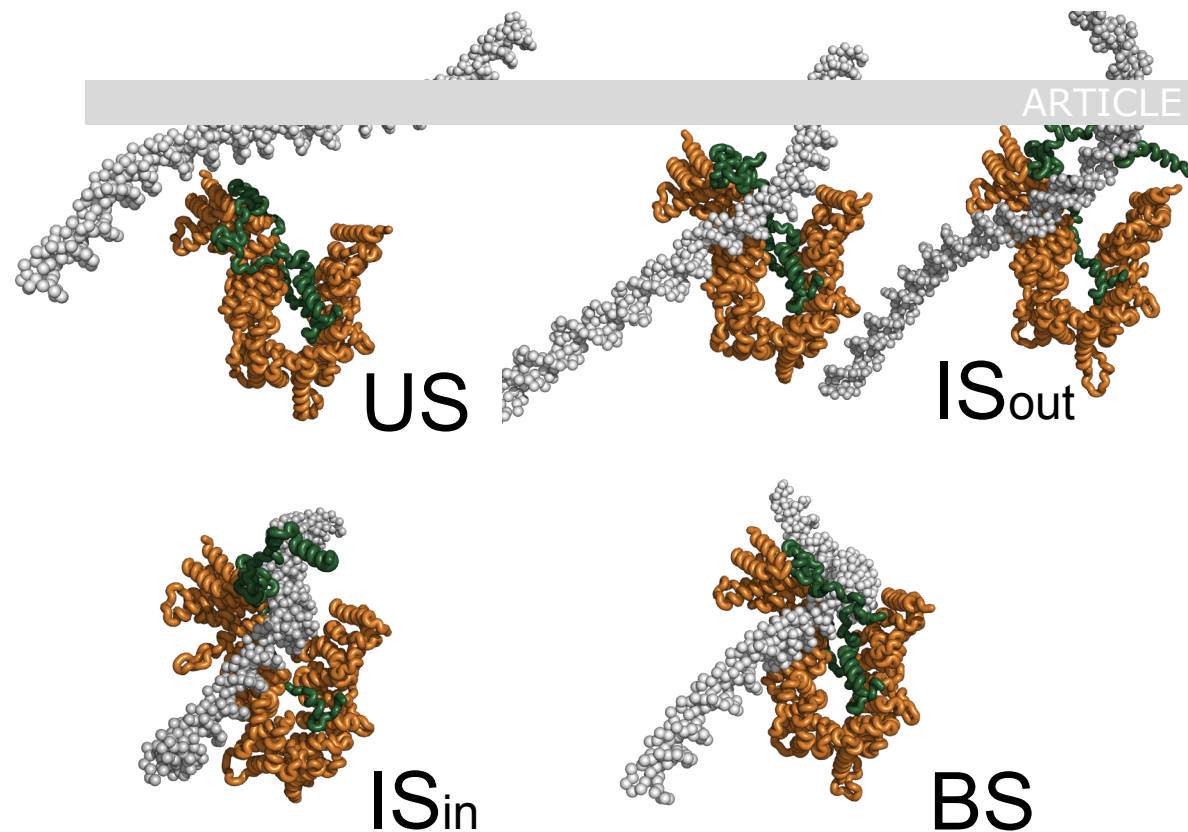
B



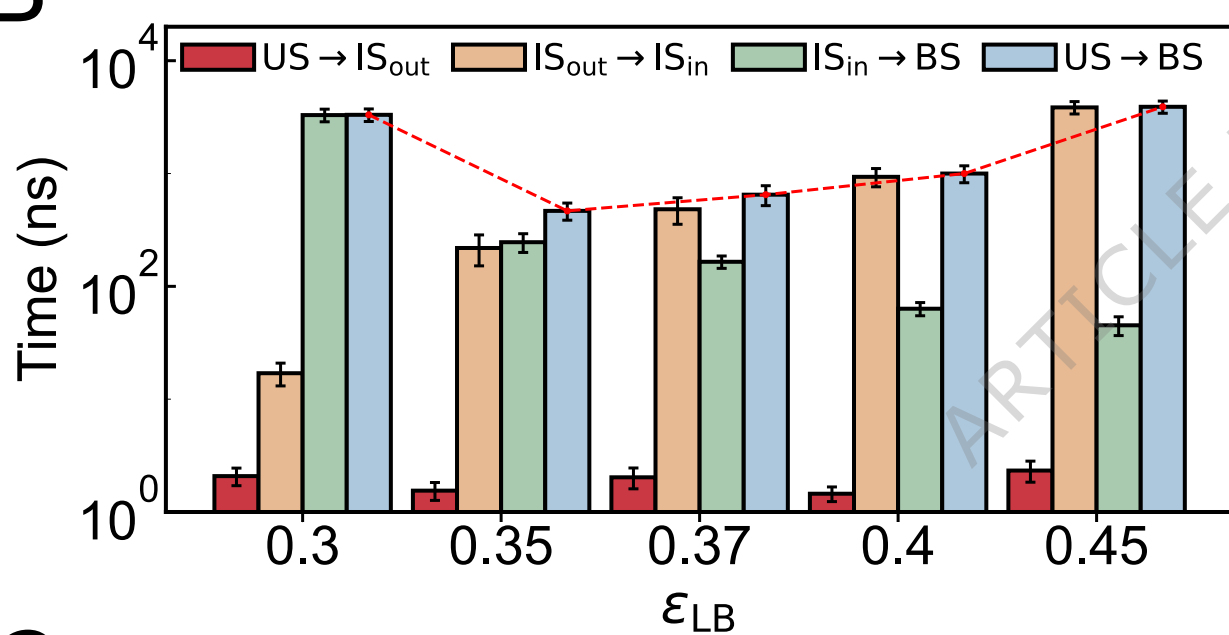
C



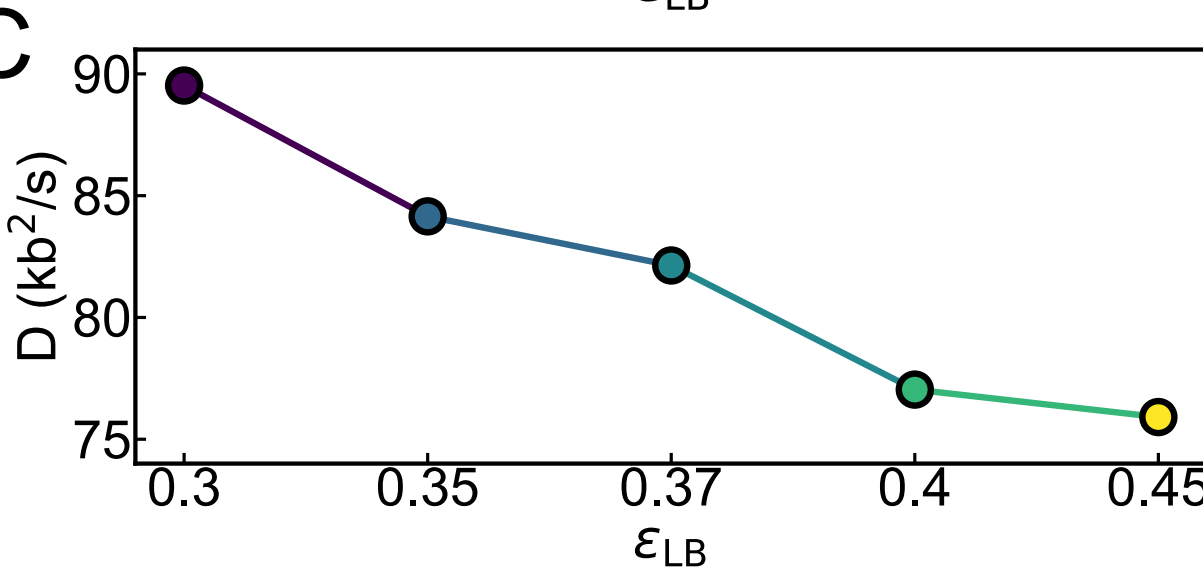
A



B



C



D

